Measurement of the Effective Weak-Mixing Angle $\left(\sin^2 \theta_{\mathbf{l}}^{\mathbf{eff}}\right)$ in $p\bar{p} \to Z/\gamma^* \to e^+e^-$ events at $\sqrt{S} = 1.96$ TeV

A Thesis submitted of the requirement for the degree of doctor of philosophy in physics

Siqi Yang
University of Science and Technology of China

2016 年 5 月 17 日

Abstract

The weak mixing angle is one of the fundamental parameters in the Standard Model. It connects the electromagnetic and the weak forces. At leading order, the Standard Model has precise predictions on the relationship between the weak mixing angle and other electroweak fundamental parameters. Higher order effects can also be absorbed into an effective form of the weak mixing angle and reflected in its measured value. Therefore, precise determination of the weak mixing angle is meaningful not only as a test on the Standard Model itself, but also for the new physics searches.

However the precision of the experimental determination of the weak mixing angle is the worst one compared to other fundamental parameters in the electroweak theory. The current most precise determinations of the weak mixing angle are from the two electron-positron collider experiments: the LEP and SLD. Their relative uncertainties are around 0.1%. Even with all independent measurements combined, the relative uncertainty of the weak mixing angle is still larger than 0.06%. Moreover, the measured value from one of the best two results, the LEP using b quark production, is much larger than that from the other one, the SLD using pure lepton production. Therefore, another independent measurement with a precision close to the LEP and SLD is very meaningful.

The Fermilab Tevatron is considered to be the most favorite experiment to perform a measurement of the weak mixing angle after the LEP and SLD. It produces a large number of the Z boson events. The Z boson can further decay into leptons, with an asymmetry in the final state which is very sensitive to the weak mixing angle. More importantly, Tevatron is a proton antiproton collider. This asymmetry in the initial state is crucial to define a direction in the Z boson productions to measure the asymmetry in the final state.

However, measurement at hadron colliders is more difficult than expectation. It is limited by the data sample and large uncertainties from both Parton Distribution Functions and particle momentum reconstruction. For the past 15 years, results from both the D0 and CDF experiments at the Tevatron had not been competitive with the best LEP and SLD measurements.

This thesis presents an other measurement of the weak mixing angle. It uses $Z \rightarrow ee$ events of the full data set collected by the D0 detector. It is one of the three last remaining chances for the Tevatron to provide a precision close to the LEP and SLD (the other two are the D0 muon channel and the CDF electron channel. The CDF muon channel is not competitive due to a small acceptance of their muon detector). Before this work started, the estimated precision was still far from the LEP and SLD results. However, significant improvements are made which lead to a surprising result, $\sin^2\theta_l^{\text{eff}} = 0.23147 \pm 0.00047$. It is the most precise measurement from light quark interactions to date. It is also the first time that weak mixing angle measured from hadron collider experiments have a precision close to the best LEP and SLD results.

摘要

弱混合角是标准模型的基本物理参数之一。它联系了电磁相互作用和弱相互作用。在树图计算中，标准模型给出了弱混合角与其它电弱基本参数之间的严格关系；在高阶计算中，高阶效应可以通过顶点过程吸收到弱混合角的有效形式中。因此，精确测量弱混合角，无论对于精确检验现有模型还是新物理的寻找都具有重要的意义。

但是，弱混合角的实际测量精度却是所有电弱基本参数中最差的一个。目前精度最好的两次弱混合角测量来自于同为正反电子对撞实验的 LEP 和 SLD。它们的相对测量精度，也仅达到千分之一而已。即使将全世界所有弱混合角的测量合并起来，相对误差也大于万分之六。而且，LEP 与 SLD 给出的两个最精确结果的测量值之间还有巨大的偏差。综上所述，对于弱混合角急需新的高精度实验测量。

美国费米国家实验室的高能对撞机 Tevatron 是继 LEP 与 SLD 结果之后被物理学界认为最有利于测量弱混合角的实验。首先，它能产生大量的 Z 玻色子。Z 玻色子的衰变是纯粹的弱相互作用，并且在末态存在空间不对称性。这个不对称性是严格被弱混合角控制的，因此很敏感。另外，Tevatron 是质子-反质子对撞机。这种不对称的初态有利于规定一个物理方向，为测量末态的不对称性提供了巨大方便。

不过在强子对撞实验上进行精确测量要比预期困难得多。统计量严重受限、系统误差巨大，都是难以克服的问题。在过去的十五年中，Tevatron 上两个主要探测器，D0 和 CDF 都在不断尝试进行弱混合角的测量。但是测量精度始终无法接近 LEP 与 SLD 的水平。

这篇博士论文介绍了 D0 实验上对弱混合角的又一次测量。这次测量使用了 D0 探测器收集到的全部 Z 衰变到电子的数据。因为全部数据都已经使用并且 Tevatron 已经停止运行，因此这次测量也是最后的有可能在 Tevatron 上达到与 LEP 和 SLD 接近精度的仅存的三个测量之一（另外两个是 D0 $Z \to \mu\mu$ 全部数据测量和 CDF $Z \to ee$ 全部数据测量。CDF 的 $Z \to \mu\mu$ 测量由于它们的 muon 探测器几何尺寸太小而无法达到相应水平）。在这片论文的工作开始之前，预计最终误差仍然是远远差于 LEP 和 SLD 的结果。不过由于统计量和电子能量刻度水平的飞跃性提高，最终测量结果令人惊喜地达到了接近 LEP 与 SLD 的水平，成为最精确的从轻夸克得到的测量结果，也是第一次能够在强子对撞上实现了与 LEP 和 SLD 接近的精度。

致谢

在我的博士阶段工作结束之时，我希望能借此机会对各位帮助过我的人表达由衷的感谢。

首先我要感谢我的导师韩良教授。我从本科阶段开始就跟随他进行学习工作，到现在为止整整十年。从最开始不计较成绩高低愿意收我为学生，到后来一步一步引领我在粒子物理实验领域前进，不断改正我的缺点，想方设法发挥我的长处，到最后将我培养成能够在本领域独当一面的合格博士生，韩老师付出了巨大的心血。我的博士阶段能够负责具有如此重要物理意义的工作，也是韩老师为我提供的机会。尤其是在我研究电子能量刻度却面临难处，长时间毫无头绪的时候，他首先以极其敏锐的物理直觉判断出该项工作最终一定是可解决的，然后对我报以巨大的信心让我无论如何接着做下去，这才有了之后的工作的整体突破。在这十年间，韩老师以极为自由的学术风格包容我以自己的方式进行学习和研究，却同时以严格的标准要求我的工作细节。这样的教育方式对我本人是极为有针对性的，也是最为有效的，不仅发挥了我愿意深究探索的性格长处，也遏制了我得过且过、粗心大意、不在意细节的毛病。这十年将一直影响我的科研生涯，是我今后进行进一步研究工作的绝对基础。

然后，我要感谢我的师兄尹航教授。从我刚开始接触 D0 实验上的研究开始，他以手把手的方式带着我一路走了过来，把多年的心得体会一点一点教给我。我的博士工作在粒子物理实验中属于最复杂、最精细的物理分析，是师兄教会我每一个细小的方法和技巧。在我的博士学习过程中，师兄是在科研最前线线对我影响最大、帮助最多、意义最重要的人。

之后，我要感谢 D0 合作组的所有成员。尤其是费米实验室的 Dmitri Denisov 博士和 Stony Brook 大学的 Paul Grannis 教授。他们二人身为合作组最高领导人，却对我的物理分析提供了近乎无微不至的帮助与关心。我的工作投稿给 PRL 以后，受到了严苛的评审，过程持续了整整一年。在此期间，他们二人一方面不断帮我争取文章的最终发表，也直接的参与到各种研究工作中。Paul Grannis 教授甚至亲自整理撰写了详尽的资料帮助我回答评审问题。这不仅让我的工作最终顺利发表，而且让我进一步学到了更多的物理知识，感受实验原则。当然，除了两位的帮助，还有 electroweak group 的 Breese Quinn 教授、Heidi Shellman 教授、谢云鹤博士、卜雪冰博士以及其他长辈、师兄和同事们。他们对我都有巨大的影响。

另外，我要感谢在科大的老师与同学们。尤其是刘明辉和宋弘烨。与他们的日常交流和相处不仅是激发想法的重要途径，也是在繁重的科研任务中保持轻松愉快的心态的主要方式。

同时，我要感谢我的妻子左阳。她以同是博士的身份，单方面地对我提供支持与照顾。或许由于专业领域不同，她并未直接对我的工作提出意见或者给出指导，但是她却营造了数年如一日的温和愉快的气氛。没有这份温柔与支持，我无法在繁重的工作中保持愉快的心理状态，更无从谈起能有自己的创新和想法了。

最后我要感谢父母。就好像跟随韩良老师学习的十年会影响我之后的科研生涯一样，我现在所有的能够帮助我克服困难的能力和品质，都是他们像设计精密仪器一样仔细规划的教育实现的。这些，都是我跨入科研领域之前就打下的基础，也是前行路上最重要的保障。

Publications and Conference talks

Conference Presentations

- Invited talk at APS April Meeting 2012 (April 2, 2012): Measurement of the forward-backward charge asymmetry in $Z/\gamma^* \to e^+e^-$ events with the D0 detector at the Tevatron.

- Invited talk at 37th International Conference of High Energy Physics 2014 (July 4, 2014): Measurements of the W charge asymmetry, the weak mixing angle and Z ϕ^* in $p\bar{p}$ collisions with the D0 detector.

- Invited talk at 3rd annual conference on Large Hadron Collider Physics (Sept. 4, 2015): Forward-backward asymmetry and $\sin^2\theta_W$.

- Major D0 internal talks:

  - "CPS variables for e/γ MC", EMID group meeting. USTC, April, 2010
  - "$W\mu\mu\,\gamma$", Diboson meeting, USTC, Sept. 2010
  - "Inter-phi calibration", CALGO meeting, 9 talks from Oct. 2010 to Oct. 2011
  - "Lumi and scale correction", EMID group meeting, Fermilab Sept. 2011
  - "A_{FB} and $\sin^2\theta_W$", D0 Workshop, 6 talks from 2012 to 2015
  - "Z mumu A_{FB}", Top-Higgs-Electroweak meeting, Jan., 2016

Publications

- Primary author of the following D0 publications:

  - $W\gamma$ production and Limits on Anomalous $WW\gamma$ Couplings in pp Collisions at $\sqrt{s} = 1.96$ TeV,
    Phys. Rev. Lett. **107**, 112005(2011).
  - Measurement of the effective weak mixing angle in $p\bar{p} \to Z/\gamma^* \to e^+e^-$ events,
    Phys. Rev. Lett. **115**, 041801(2015).

- Primary author of internal Notes:

  - "$p\bar{p} \to W\gamma + X$ with W decays to muon", D0 Note 6142 (Jan. 2011)
  - "$W\gamma$ production at DZero with L=4.2 fb^{-1} data", D0 Note 6172 (Feb. 2011)
  - "$W\gamma$ production in electron channel with L=4.2 fb^{-1} data", D0 Note 6221 (Feb. 2011)
  - "A novel method for the electron energy calibration at D0", D0 Note 6413 (Dec. 2013)
  - "Measurement of the Effective Weak-Mixing angle in $p\bar{p} \to Z\gamma^* \to e^+e^-$ events at 1.96 TeV", D0 Note 6426 (March, 2014)

Contents

4

List of Figures

8

9

List of Tables

Chapter 1

Introduction

One of the main goals of particle physics is to understand what matter is made of, and what are the forces in nature through which matter interacts. Our current understanding of the fundamental forces and elementary particles is described by the Standard Model (SM) of particle physics. The SM describes the fundamental units of matter as spin-$\frac{1}{2}$ leptons and quarks. Leptons and quarks are interacting via gauge bosons: the photon (γ), the $W^{\pm}$ and Z^0, and the gluon (g), mediating the corresponding electromagnetic, the weak and the strong forces.

The SM provides a very elegant theoretical framework and has been successfully tested by experiments. Almost all experimental results, with an energy scale from MeV to TeV, are consistent with the SM predictions. On one hand, it is good to have such successful and relative simple model; On the other hand, physicists get very few cues for existence of new physics beyond the SM. In this case, it is meaningful to precisely measure those fundamental parameters in the SM. Any sensible deviation observed in experiments could provide clues for the new physics search.

One of the most interesting precise measurements is the determination of the weak mixing angle. The weak mixing angle defines the ratio between the electromagnetic and weak forces in the electroweak theory [1]. Besides, higher order effects (section 1.1) can be absorbed into an effective shift on the weak mixing angle and reflected on its experimental measured value. However, the precision of the experimental determination of the weak mixing angle is the worst compared to other fundamental parameters in the electroweak theory, which are the fine structure constant α (relative uncertainty $\delta \sim 4 \times 10^{-8}$) measured from the quantum Hall effect, the Fermi coupling constant G_F ($\delta \sim 2 \times 10^{-5}$) measured from the muon lifetime and the Z boson mass M_Z ($\delta \sim 2 \times 10^{-5}$) measured by the LEP ee collision experiment. For the weak mixing angle, the best two results, one from the LEP experiment measuring 0.23221 ± 0.00029 and the other one from the SLD experiment giving 0.23098 ± 0.00026 [2], just achieve a precision around 0.1%. Moreover, results from the LEP and SLD have a tension of 3.2 standard deviation. Therefore, an independent measurement on the weak mixing angle is very meaningful.

After the LEP and SLD gave their best results on the weak mixing angle, the proton-antiproton collider Tevatron is the most favorable to achieve improvement. Before Tevatron RunII, Physicists had estimated the uncertainty on the weak mixing angle. Theoretical estima-

tion predicted an uncertainty of 0.0005, with 10 fb^{-1} data that would be accumulated in electron channel at D0 experiment. It is considered to be close to the best LEP and SLD results. The first attempt was made using 1 fb^{-1} data in electron channel [3]. Although the uncertainty was large, it showed feasibility of such a precise a measurement at hadron colliders. Three years later, a measurement using 5 fb^{-1} data in electron channel, 0.2309 ± 0.0010, was published [4]. The results was much better and surpassed the LEP combination of inclusive hadronic results (not the most precise one mentioned above. That is the LEP combined b quark result).

However, based on the accumulation of the integrated luminosity and the 5 fb^{-1} result, the uncertainty using 10 fb^{-1} data is estimated to be larger than 0.0008. It is far from the 0.0005 expectation. On one hand, it is very difficult to make experimental improvements; One the other hand, precise measurement at Tevatron is badly needed because if Tevatron has no significant improvements, it will be even more difficult to measure the weak mixing angle at the Large Hadron Collider (LHC) due to dilution effect in proton-proton collision.

Under such tricky and complicated circumstance, the work of this thesis has been carried out. It focus on the measurement of the weak mixing angle in $Z \to e^+e^-$ events using full data set collected by the D0 detector. It is exciting that the precision finally achieves the goal of 0.0005. The improvements are made by introducing a new method on precise electron energy calibration. This calibration, not only reduces the systematic uncertainty due to energy measurement, but also allows to use those electrons that had always been excluded from the D0 precise measurements due to poor reconstruction.

The thesis will first give a brief introduction to the weak mixing angle and the previous measurements (Chapter 1), followed by a view of the D0 detector (Chapter 2). Chapter 3 is a general outline of the measurement strategy. Chapter 4 - 8 describe the details of the measurements. The new energy calibration method is discussed in Chapter 5. The uncertainties and final results are discussed in Chapter 9, followed by Chapter 10 summarizing the whole thesis.

1.1 The Electroweak theory and the Weak mixing angle

The electromagnetic force and the weak force are described by a unified electroweak theory of Glashow, Salam andWeinberg [1]. Leptons, including (e, ν_e), (μ, ν_μ) and (τ, ν_τ) are assigned to a left handed doublet and a right handed singlet. For example:

$$
\begin{aligned}
R_e &= (e)_R \\
L_e &= \begin{pmatrix} \nu_e \\ e \end{pmatrix}_L
\end{aligned}
\tag{1.1}
$$

where left handed and right handed are components of a field ψ defined as

$$
\begin{aligned}
\psi_R &= \frac{1 - \gamma_5}{2} \psi \\
\psi_L &= \frac{1 + \gamma_5}{2} \psi
\end{aligned}
\tag{1.2}
$$

The weak charge current interaction is parity-violating and connects the left handed states:

$$
\begin{aligned}
J_\mu^+ &= \bar{\nu}\gamma_\mu \frac{1+\gamma_5}{2} e = \bar{\psi}_L \gamma_\mu \tau^+ \psi_L \\
J_\mu^- &= \bar{e}\gamma_\mu \frac{1+\gamma_5}{2} \nu = \bar{\psi}_L \gamma_\mu \tau^- \psi_L
\end{aligned}
\tag{1.3}
$$

where $\tau^\pm = \tau_1 \pm \tau_2$ are the Pauli operators. And the neutral current can be:

$$
J_\mu^3 = \bar{\psi}_L \gamma_\mu \tau_3 \psi_L.
\tag{1.4}
$$

The Lagrangian which describes the electroweak unification can be written as:

$$
L = g\mathbf{J}_\mu \cdot \mathbf{W}_\mu + g' J_\mu^Y B_\mu
\tag{1.5}
$$

where $\mathbf{W}_\mu = W_\mu^1, W_\mu^2, W_\mu^3$ are gauge fields of the $SU(2)_L$ group and B_μ is the gauge field of the $U(1)_Y$ group. g and g' are couplings of fermions to $\mathbf{W}_\mu$ and B_μ fields. $\mathbf{J}_\mu = J_\mu^1, J_\mu^2, J_\mu^3$ and J^Y are isospin and hypercharge currents of fermions. The hypercharge, Y, is defined as:

$$
\frac{Y}{2} = Q - I_3
\tag{1.6}
$$

where Q is the charge and I_3 is the third component of weak isospin. The lagrangian in Eq 1.5 can be re-written just in another form to directly describe the charge-changing current, the neutron current and the electromagnetic current processes observed in experiments:

$$
L = \frac{g}{\sqrt{2}}(J_\mu^- W_\mu^+ + J_\mu^+ W_\mu^-) + \frac{g}{\cos\theta_W}(J_\mu^3 - \sin\theta_W J_\mu^{\text{em}})Z^\mu + g\sin^2\theta_W J_\mu^{\text{em}} A_\mu
\tag{1.7}
$$

where we have

$$
\begin{aligned}
W_\mu^\pm &= \frac{1}{\sqrt{2}}(W_\mu^1 \pm i W_\mu^2) \\
Z_\mu &= W_\mu^3 \cos\theta_W - B_\mu \sin\theta_W \\
A_\mu &= W_\mu^3 \sin\theta_W + B_\mu \cos\theta_W \\
J_\mu^{\text{em}} &= J_\mu^Y - J_\mu^3 \\
J_\mu^\pm &= J_\mu^1 \pm i J_\mu^2 \\
\tan\theta_W &\equiv \frac{g'}{g}
\end{aligned}
$$

By doing this, $W_\mu^\pm$ and Z_μ represent the $W^\pm$ and Z^0 bosons observed as intermediators of the weak force while A_μ is the photon corresponding to the electromagnetic force. This is how the electromagnetic and weak forces "mix" into a unified $SU(2)_L \times U(1)_Y$ theory. The weak mixing angle, defined as θ_W, represents the relative contribution from the electromagnetic and weak forces when they "mix". As the connection between these two forces, its importance can be expressed in other way:

$$
\sin\theta_W = \frac{e}{g}.
\tag{1.8}
$$

13

Specifically, at tree level the vector and axial vector couplings of the Z boson with fermions can be expressed by the fermion charge Q and the third component of weak isospin I_3^f:

$$
\begin{aligned}
g_V^f &= I_3^f - 2Q_f \sin^2\theta_W \\
g_A^f &= I_3^f.
\end{aligned}
\tag{1.9}
$$

Radiative corrections to the propagators and vertices, as shown in Fig. 1.1 and Fig. 1.2, can be absorbed up to all orders into an overall scale ρ_f and a shift κ_f on the weak mixing angle $\sin^2\theta_W$ by re-writing Eq. 1.9 as

$$
\begin{aligned}
\mathfrak{g}_V^f &= \sqrt{\rho_f}(I_3^f - 2Q_f\kappa_f \sin^2\theta_W) \\
\mathfrak{g}_A^f &= \sqrt{\rho_f}I_3^f.
\end{aligned}
\tag{1.10}
$$

The effective weak mixing angle related to the flavour of the fermions is then defined as:

$$
\sin^2\theta_f^{\text{eff}} = \kappa_f \sin^2\theta_W.
\tag{1.11}
$$
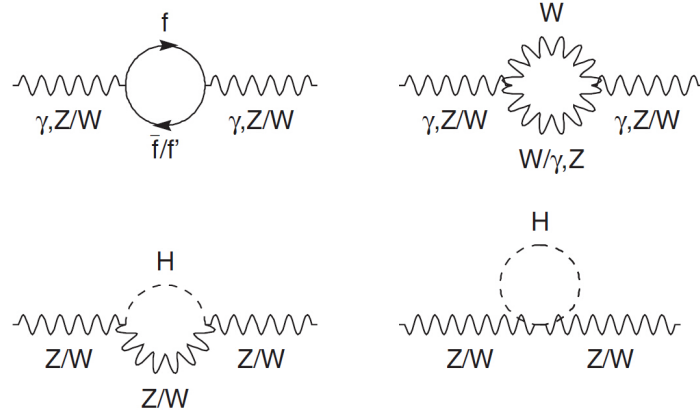
Figure 1.1: Higher order corrections due to boson and fermion loops.
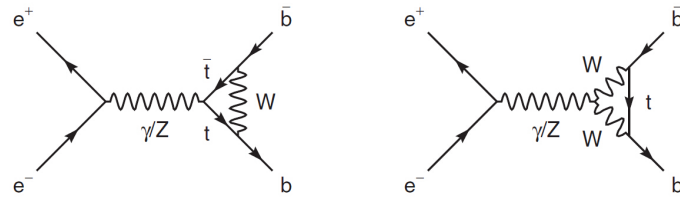
Figure 1.2: Vertex corrections to the fermions in the final states in an example of $b\bar{b}$ production.

1.2 Drell-Yan process and A_{FB}

The Drell-Yan process at parton level is $q\bar{q} \to Z/\gamma* \to e^+e^-$. The differential cross section for this process at tree level is:

$$
\begin{aligned}
\frac{d\sigma}{d\cos\theta} &\sim Q_e^2 Q_q^2 (1+\cos^2\theta) + Q_e Q_q Re(\chi(s)) \left[2g_V^q g_V^e (1+\cos^2\theta) + 4g_A^q g_A^e \cos\theta \right] \\
&+ |\chi(s)|^2 \left[(g_V^{q\,2} g_A^{q\,2})(g_V^{e\,2} g_A^{e\,2})(1+\cos^2\theta) + 8g_V^q g_V^e g_A^q g_A^e \cos\theta \right] \\
&= A(1+\cos^2\theta) + B\cos\theta
\end{aligned}
\tag{1.12}
$$

where $g_V^f = I_3^f + 2Q_f \sin^2\theta_W$ and $g_A^f = I_3^f$ are the vector and axial-vector couplings related to the third component of weak isospin I_3^f. θ is the scattering angle between the directions of incoming quarks and outgoing leptons with negative change. $\chi(s)$ is expressed as:

$$
\chi(s) = \frac{1}{\cos^2\theta_W \sin^2\theta_W} \frac{s}{4 \times (s - M_Z^2 + i\Gamma_Z M_Z)}.
$$

The existence of term $B\cos\theta$ in the differential cross section leads to an asymmetry between the forward events, which are defined as $\cos\theta > 0$ and backward events, which are defined as $\cos\theta < 0$. The forward-backward charge asymmetry, A_{FB}, is defined to describe how large it is:

$$
\begin{aligned}
A_{FB} &\equiv \frac{\sigma_F - \sigma_B}{\sigma_F + \sigma_B} \\
&= \frac{\int_0^1 \frac{d\sigma}{d\cos\theta} d\cos\theta - \int_{-1}^0 \frac{d\sigma}{d\cos\theta} d\cos\theta}{\int_0^1 \frac{d\sigma}{d\cos\theta} d\cos\theta + \int_{-1}^0 \frac{d\sigma}{d\cos\theta} d\cos\theta} \\
&= \frac{3}{8}\frac{B}{A} \\
&= A_{FB}(\sin^2\theta_W, \sqrt{s}) \\
&= A_{FB}(\sin^2\theta_W, M_{ee}).
\end{aligned}
\tag{1.13}
$$

A_{FB} as a function of $\sin^2\theta_W$ in Eq. 1.13 is shown in Fig. 1.3. Note that the relationship is not exactly linear, but approximately a straight line. The sensitivity represented by the slope of the "straight" line depends on the $\sqrt{s}$ of the process. Fig. 1.4 shows the sensitivity in $u\bar{u}$ and $d\bar{d}$ processes. The most sensitive range is in the vicinity of the Z boson pole, but the largest sensitivity does not exactly appear at the peak value of Z boson mass. So A_{FB}, or A_{FB} as a function of the invariant mass of the di-electrons in the final state (shown in Fig. 1.5), is the favourite observable to extract the weak mixing angle especially at hadron colliders.

15
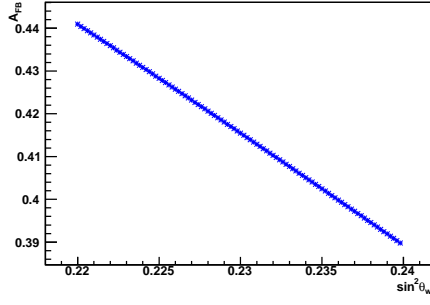
Figure 1.3: The standard model leading-order (LO) prediction of A_{FB} as a function of $\sin^2\theta_W$ at $\sqrt{s} = 90$ GeV for $u\bar{u} \to e^+e^-$ events.
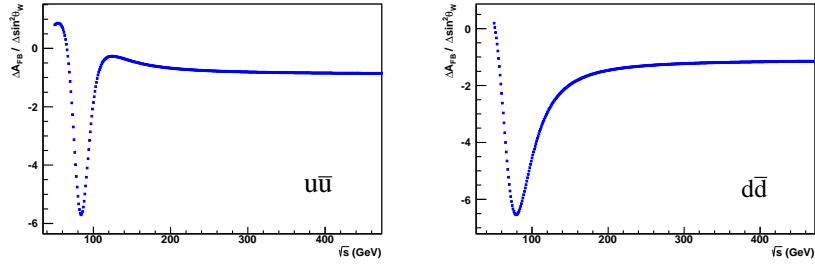
Figure 1.4: Sensitivity of A_{FB} vs. $\sin^2\theta_W$ as a function of $\sqrt{s}$ in $u\bar{u}$ (left) and $d\bar{d}$ processes (right).
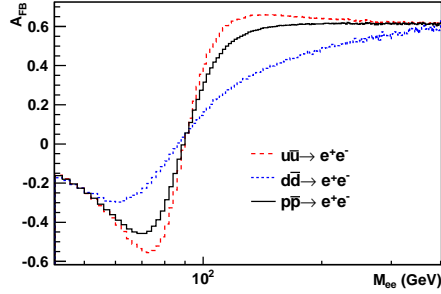
Figure 1.5: The standard model leading-order (LO) prediction of A_{FB} as a function of invariant mass.

In this measurement, forward and backward categories are determined in the emission angle (θ^*) defined in the Collin-Soper frame [5]:

$$\cos\theta^* = \frac{2}{Q\sqrt{Q^2 + Q_T^2}}(P_1^+ P_2^- - P_2^+ P_1^-) \tag{1.14}$$

where $Q(Q_T)$ is the four momentum (transverse momentum) of the lepton pair, $P_i^{\pm} = \frac{1}{\sqrt{2}}(P_i^0 \pm P_i^3)$, and P^0 and P^3 represent the energy and the longitudinal component of the lepton momentum. Events with $\cos\theta^* > 0$ are classified as forward (F), and those with $\cos\theta^* < 0$ are as

16

backward (B). A_{FB} is observed using the number of forward and backward events:

$$A_{FB} = \frac{N_F - N_B}{N_F + N_B}. \tag{1.15}$$

1.3 Previous experiments

Precise determinations of $\sin^2\theta_l^{\text{eff}}$ at an energy scale around Z resonance have been done at the LEP and SLD experiments [2] in various processes. One of the most precise results is the combined LEP measurement using the forward-backward asymmetry for $e^-e^+ \rightarrow b\bar{b}$ production ($A_{FB}^{0,b}$), measuring $\sin^2\theta_l^{\text{eff}} = 0.23221 \pm 0.00029$. Another one is from the SLD measurement of the left-right polarization asymmetry A_{lr} for $e^+e^- \rightarrow e^+e^-$ process, giving $\sin^2\theta_l^{\text{eff}} = 0.23098 \pm 0.00026$. These two results are dominated by the statistical uncertainties. A tension of 3.2σ lies between the most two precise measurements. Most interestingly, the LEP measurement contains both Z to lepton and Z to quark couplings while the SLD measurement is related only to the Z-lepton couplings. The average, 0.23153 ± 0.00016, is the combination of e^+e^- collider results.

At the fermilab Tevatron, the CDF experiments have independently measured the weak mixing angle, both in $Z \rightarrow e^-e^+$ [6, 7] and $Z \rightarrow \mu^-\mu^+$ [8] channels. The latest previous D0 measurement in $Z \rightarrow e^+e^-$ events using 5 fb^{-1} of data, $\sin^2\theta_l^{\text{eff}} = 0.2309 \pm 0.0008(\text{stat.}) \pm 0.0006(\text{syst.})$, was published in 2011 [4]. These measurements are dominated by the statistical uncertainties and the Parton Distribution Functions (PDFs) which describe the momentum of quarks in the hadrons. Besides, the systematic uncertainties due to lepton momentum measurement, backgrounds estimation and others are larger compared to the e^-e^+ collider experiments. At the Large Hadron Collider (LHC), measurements of $\sin^2\theta_l^{\text{eff}}$ have been reported by the ALTAS and CMS Collaboration [9, 10]. However, their results are not competitive with Tevatron due to large effect of dilution.

In general, the best results are from the LEP and SLD lepton collider experiments. Results from hadron colliders are limited by the data sample, the large uncertainty from PDFs and systematics. The comparison between previous meausrements is shown in Fig. 1.6.

LEP and SLD Average
0.23153 ± 0.00016

$A_{fb}^{0,l}$	**0.23099 ± 0.00053**
$A_l(P_\tau)$	**0.23159 ± 0.00041**
A_{lr} **(SLD)**	**0.23098 ± 0.00026**
$A_{fb}^{0,b}$	**0.23221 ± 0.00029**
$A_{fb}^{0,c}$	**0.23220 ± 0.00081**
Q_{fb}^{had}	**0.2324 ± 0.0012**
A_{FB}^{ee} **(CDF), 2.0 fb^{-1}**	**0.2328 ± 0.0011**
$A_{FB}^{\mu\mu}$ **(CDF), 9 fb^{-1}**	**0.2315 ± 0.0010**
A_{FB}^{ee} **(DØ), 5.1 fb^{-1}**	**0.23090 ± 0.00100**

0.228   0.23   0.232   0.234   0.236   0.238

$$\sin^2 \theta_{eff}^l$$
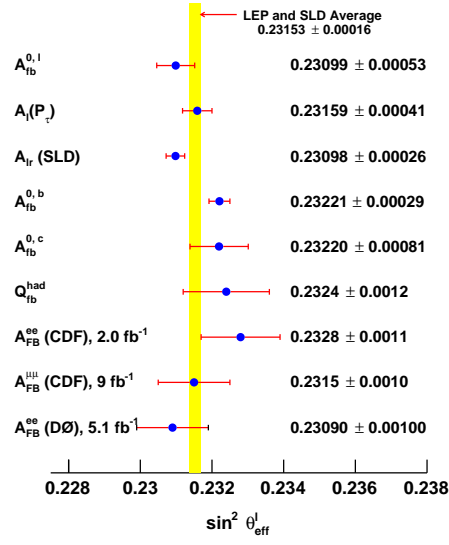
Figure 1.6: Previous measurements of $\sin^2 \theta_l^{\mathrm{eff}}$ from other experiments.

Chapter 2

Experimental Apparatus

2.1 The D0 detector

The D0 detector is designed as a multi-purpose detector [11, 12, 13] at the Fermilab Tevatron, which is a proton-antiproton collider. Fig. 2.1 shows an overview of the detector. In general, it has a tracking system at the most inner side of the detector, a nearly 4π solid angle uranium liquid-Argon calorimeter and a muon spectrum at the most outside. Tracks of electrons are reconstructed in the tracking system, and are further used to determine the directions and charges of electrons and the position of the $p\bar{p}$ interaction point (primary vertex). The determination of electron energy uses only the information from the calorimeter.

The d0 coordinate system is defined as following: The direction of the proton beam is defined as $+z$ pointing from north to south. The $+y$ direction points up. The $+x$ direction is then defined to form a standard right-handed coordinate system. A cylindrical coordinate system is further used by introducing the polar angle θ and the azimuthal angle ϕ. The dimension represented by θ is usually expressed as rapidity Y:

$$Y = \frac{1}{2} \ln \left(\frac{E + p_z}{E - p_z} \right)$$

where E and p_z are the energy and z component of the momentum of a particle. In the limit $p \gg m$, Y can be approximately written as

$$\eta \equiv -\ln \left[\tan \frac{\theta}{2} \right].$$

Since the energy of the incoming protons and antiprotons is very large (980 GeV each), the $p \gg m$ limit is proper for photons and all leptons. W and Z bosons are not considered in this limit because their mass cannot be ignored. For particles, Y or η represents the physics directions with respect to the primary vertex. A pseudorapidity η_{det} is used to describe the position with respect to the center of the detector.
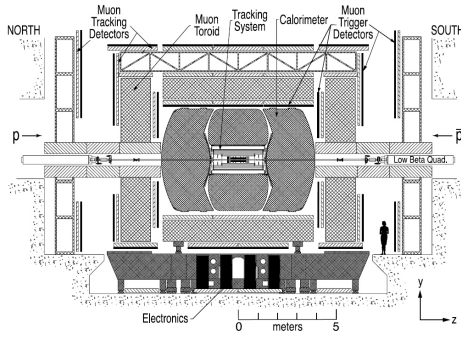
Figure 2.1: The D0 detector.

2.1.1   Tracking System

The D0 tracking system is comprised of the Silicon Microstrip Tracker (SMT) and the
3 Central Fiber Tracker, shown in Fig. 2.2. Both SMT and CFT are surrounded by a 1.9 Tesla
superconducting solenoid magnet. The SMT consists of 6 barrels with interspersed disks. As
the closet detector to the beamline, it provides the highest position resolution of approximately
6 10 μm. The SMT has a coverage of $|\eta_{\mathrm{det}}| \sim 3$. The CFT is the next closet subsystem to the
beamline. It has 8 super-layers. Each super-layer has doublet layers of scintillating fibers. The
CFT helps the SMT in tracking reconstruction with a coverage of $|\eta_{\mathrm{det}}| \sim 2$.
9 The number of hits in the SMT and CFT used in the reconstruction is significant to the
quality of tracks. Although the determination of electron energy is independent with SMT
and CFT, it is important to have high quality tracks matching to electrons. The charge mis-
12 identification probability of electrons is smaller with high quality tracks. Backgrounds can also
be suppressed by the strict requirements on the quality of matched tracks.

The polarity of the solenoid magnetic field is regularly reversed every two weeks on average.
15 By doing this, potential difference in the reconstruction between e^{+} and e^{-} is suppressed.
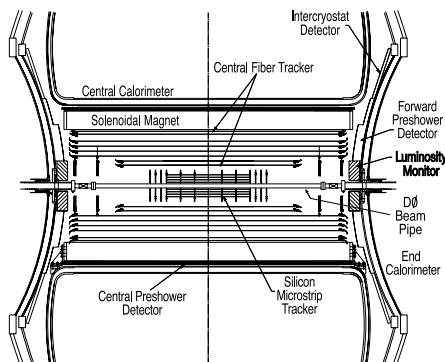
Figure 2.2: Cross-sectional view of the D0 tracking system.

2.1.2 Calorimeters

The D0 calorimeters are the most important subsystem to the electron-based measurement. They located outside the tracking system, shown in Fig. 2.3. The Central Calorimeter (CC) covers $|\eta_{\mathrm{det}}| < 1.1$, and two Endcap Calorimeters (EC) cover $1.5 < |\eta_{\mathrm{det}}| < 3.5$. Gaps between $1.1 < |\eta_{\mathrm{det}}| < 1.5$ are covered by the InterCryostat Detector (ICD), but not used in this measurement due to poor energy resolution. The first four layers in the CC and EC are the EM section, with transverse segmentation of $\Delta\eta \times \Delta\phi = 0.1 \times 0.1$. The third layer of the EM calorimeter (EM3) has a finer segmentation of 0.05×0.05 which can help locating the position of reconstructed electrons in the detector. Outside the EM section is the hadronic section measuring energy of jets. The minimal segmentation in each layer defines a cell. Cells in different layers but with same η and ϕ are grouped together to form towers.

Electrons lost energy in the EM section of the calorimeters via pair production ($\gamma \to e^+e^-$) and bremsstrahlung ($e \to e\gamma$). The energy lost is described by:

$$E(x) = E_0 e^{-\frac{x}{X_0}} \tag{2.1}$$

where E_0 is the original energy of electron, x is the distance traveled in the calorimeter and X_0 is the radiation length of the material. For uranium, $X_0 \approx 3.2$ mm. Electrons pass through materials about $1.8 - 5 \ X_0$ before they arrive the EM calorimeter.

Electrons and photons are reconstructed as EM clusters by detecting localized energy deposits in the EM calorimeter and the first hadronic layer (FH1). In the CC, the tower with the highest transverse energy (further required $E_T > 500$ MeV) is selected as the center of this EM cluster. Towers in a cone of radius $R = \sqrt{(\Delta\eta)^2 + (\Delta\phi)^2}$ around the selected center tower are used to form the EM cluster. In the EC, an initial cell with the highest energy content in the EM3 layer is selected as the center of the EM cluster. Cells with a transverse distance of < 10 cm from the selected center cell are used in the cluster reconstruction. The resolution of the calorimeters can be described as:

$$\frac{\sigma_E}{E} = \sqrt{\left(\frac{N}{E}\right)^2 + \left(\frac{S}{\sqrt{E}}\right)^2 + C^2} \tag{2.2}$$

where N, S and C represent noise, sampling and constant terms.
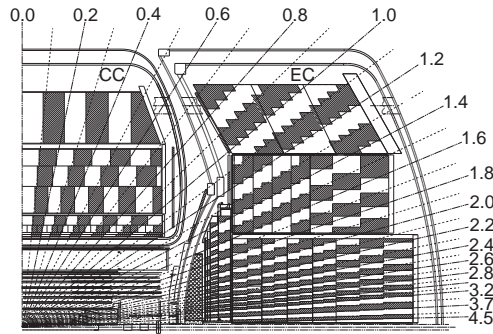
Figure 2.3: Side view of one quadrant of the D0 calorimeters.

Chapter 3

Measurement Strategy

3.1 Improvements from previous analysis

U. Baur gave an estimation on the total uncertainty of the weak mixing angle with 10 fb^{-1} data before Tevatron RunII [14]. The estimated uncertainties on the $Z \to e^+e^-$ channel are listed in Tab. 3.1.

	U. Baur's estimation on 10 fb^{-1}	D0 5 fb^{-1}	10 fb^{-1} same strategy as 5 fb^{-1}
acceptance	$\lvert\eta_{\mathrm{det}}\rvert < 1.1$	$\lvert\eta_{\mathrm{det}}\rvert < 1.0$(CC) $1.1 < \lvert\eta_{\mathrm{det}}\rvert < 2.5$ (EC) exclude EC-EC events	same
efficiency	100%	$\sim 50\%$	same
uncertainties			
statistical	0.0005	0.0008	0.0006
PDF	0.00018	0.00048	0.00048
electron energy	negligible	0.00029	0.00021
others	negligible	0.00021	0.00015
total uncertainty	0.0005	0.0010	0.00081

Table 3.1: Uncertainties on $\sin^2\theta_{\mathrm{l}}^{\mathrm{eff}}$.

As shown in Tab. 3.1, the overall acceptance × efficiency is much worse than the value used in the estimation. Systematic uncertainties are also underestimated. The uncertainty of 10 fb^{-1} measurement, if using the same strategy from 5 fb^{-1} measurement, will be much larger than U. Baur's prediction.

To achieve the predicted precision, at least 60% more statistics are needed. Besides, systematic uncertainties, especially the dominant one from electron energy measurement, have to be reduced to negligible level. Several improvements are made in the 10 fb^{-1} measurement compared to the previous analysis:

- Excluded electrons are used: electrons which were reconstructed near the boundaries of CC calorimeter modules [11] (phi-mod boundary) are used for the first time. The geometric acceptance in η is extended from $|\eta_{\det}| < 1.0$ to $|\eta_{\det}| < 1.1$ for the CC, and from $1.5 < |\eta_{\det}| < 2.5$ to $1.5 < |\eta_{\det}| < 3.2$ for the EC. EC-EC events, of which both electrons are reconstructed in the EC are also included. The data sample is then enlarged by 85% over what would be expected.

- To reduce the uncertainty from electron energy measurement, especially with those poorly reconstructed electrons, a new energy calibration method is applied. By doing this, the uncertainty from energy measurement is reduced to negligible level.

- The latest NNPDF2.3 [15] is used instead of the CTEQ6 in the previous analysis. The PDF uncertainty is reduced to 0.00017.

These steps are crucial to the final results.

3.2 Measurement strategy

This analysis is done in the following steps:

- Apply event selection cuts and obtain number of selected forward and backward events for each invariant mass bin (Chapter 4)

- Apply energy calibration separately for data and Monte Carlo (MC) (Chapter 5)

- Apply other MC corrections (Chapter 6)

- Subtract QCD and other SM backgrounds from the data to get the background-subtracted raw A_{FB} distribution as a function of invariant mass (Chapter 7)

- Extract $\sin^2 \theta_l^{\text{eff}}$ using the raw A_{FB} distribution (Chapter 8)

- Estimate the uncertainties (Chapter 9)

The D0 RunII data set is separated into two parts: RunIIa and RunIIb corresponding to different run periods. The data-MC agreement is achieved by applying strategies described in Chapter 4 - 7. For brevity, details of the energy calibration, the MC corrections and background estimation are shown only with RunIIb as examples. The weak mixing angle extraction and uncertainty estimation in Chapter 8 and 9 correspond to the full RunII data set.

Chapter 4

Event Selection

4.1 Data and MC description

4.1.1 Data samples

The full 9.7 fb^{-1} data set collected by the DØ detector is used. It corresponds to the run range from 151871 to 219000 for RunIIa (corresponding to 1.1 fb^{-1}) and that from 222028 to 275727 for RunIIb (corresponding to 8.6 fb^{-1}) data. Only events which pass the standard data quality requirements are kept for the final analysis.

The weak mixing angle is separately extracted from RunIIa and RunIIb data set with same strategy. The two extracted results are further combined as the final measured weak mixing angle. The following chapters will use RunIIb data as examples.

4.1.2 Signal samples

The Monte Carlo samples of the Drell-Yan $Z/\gamma^* \to e^+e^-$ events are generated using the standard DØ simulation chain, based on the leading-order PYTHIA generator [16] with the NNPDF2.3 [15] parton distribution functions. The PYTHIA MC samples are separately generated for invariant mass from 15 to 60 GeV, 60 to 130 GeV and 130 to 250 GeV. Samples in different mass ranges are combined according to their cross sections, shown in Tab. 4.1. The weak mixing angle is finally extracted in the mass range between 75 and 115 GeV. However, the samples in larger mass range are used to understand detector responses and to tune the MC simulation.

	statistics	cross section (pb)
15 - 60 GeV	5M	525.6
60 - 130 GeV	30M	254
130 - 250 GeV	5M	1.91

Table 4.1: PYTHIA MC $Z/\gamma^* \to ee$ samples used for this measurement.

Fig. 4.1 shows the invariant mass distributions from the three mass range MC after nor-

malization using different cross sections corresponding to the mass range.
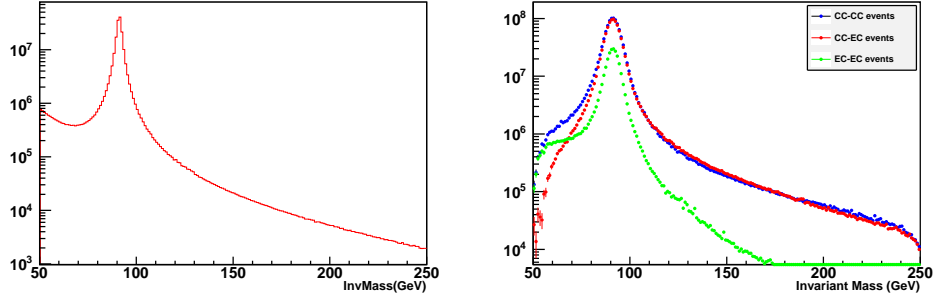
Figure 4.1: The invariant mass distributions in signal MC. left: generator level; Right: reconstruction level.

4.1.3 Background MC samples

The Pythia MC samples used to estimate the electroweak (EW) backgrounds are listed in Tab. 4.2 with the LO cross sections obtained from Pythia.

To estimate the $W + X$ background, we use Alpgen [17] + Pythia samples, shown in Table 4.3 together with LO cross sections taken from [18]. Constant next-to-leading order (NLO) k-factors of 1.30 and 1.47, predicted by [19], are applied to light quark (nlp) and heavy quark (2c and 2b) samples of $W + X$ processes respectively.

channel	xsection(pb)	statistics
$Z \to \tau\tau$ (15-60)	363.1	5M
$Z \to \tau\tau$ (60-130)	179.6	10M
$Z \to \tau\tau$ (60-130)	1.348	4M
$\gamma + \gamma$(50-130)	42.3	2M
$\gamma + \gamma$(130-250)	3.12	2M
$WW \to$ incl	8.003	5M
$WZ \to 3l + \nu$	0.07844	2M
$t\bar{t}$	6.1	2M

Table 4.2: The MC samples used for EW background studies. The LO cross sections listed here are from the Pythia generator.

25

	σ (pb)	statistics
$W(l\nu)$+0lp excl.	5885.63	90M
$W(l\nu)$+1lp excl.	1673.98	40M
$W(l\nu)$+2lp excl.	401.08	22M
$W(l\nu)$+3lp excl.	96.74	6M
$W(l\nu)$+4lp excl.	22.07	3M
$W(l\nu)$+2b+0lp incl.	13.75	3M
$W(l\nu)$+2b+1lp incl.	6.33	1.5M
$W(l\nu)$+2b+2lp incl.	2.25	74K
$W(l\nu)$+2b+3lp incl.	1.07	38K
$W(l\nu)$+2c+0lp incl.	35.87	6M
$W(l\nu)$+2c+1lp incl.	19.83	3M
$W(l\nu)$+2c+2lp incl.	8.03	1.5M
$W(l\nu)$+2c+3lp incl.	3.75	75K

Table 4.3: $W + X$ ALPGEN + PYTHIA MC samples for W+jets. The cross sections are given at LO level.

4.2   Event selection

We require two high p_T EM objects in the final state. Each of them should be in the CC or EC. The shower shapes in the calorimeter are required to be consistent with that of an electron. This is done by applying cuts on some variables, including:

- emf $= \frac{E_{\mathrm{EM}}}{E_{\mathrm{tot}}}$, where E_{EM} is the energy in the EM layers of the calorimeter and E_{tot} is the total energy. For an electron, emf should be very close to 1 while for an EM-liked jet it is much larger.

- iso $= \frac{E_{\mathrm{tot}}(R<0.4)-E_{\mathrm{EM}}(R<0.2)}{E_{\mathrm{EM}}(R<0.2)}$, where $E_{\mathrm{tot}}(R < 0.4)$ is the total energy deposited in a cone of $R < 0.4$ with respect to the center of the cluster, and $E_{\mathrm{EM}}(R < 0.2)$ is the energy in a cone of $R < 0.2$. This variable (isolation) is used to describe how large the shower is. It is smaller for an electron than an EM-liked jet.

- Hmx7 for the CC and Hmx8 for the EC are χ^2 calculated from a covariance matrix technique [20, 21, 22]. An electron has a much smaller Hmx7 or Hmx8 value than a jet.

The details of selections for EM objects are listed bellow:

- $p_T > 25$ GeV, ID $= 10, \pm 11$, emf > 0.9.

- CC electrons:

  - $|\eta_{\mathrm{det}}| < 1.1$
  - Hmx7 < 12
  - iso < 0.15

26

- track match probability > 0.0, track $p_T > 10$ GeV, track fit $\chi^2 < 9.95$, at least two SMT hits and nine CFT hits, beam-spot corrected DCA $|r_{\text{DCA}}| < 0.02$ cm

- EC electrons:

  - $1.5 < |\eta_{\text{det}}| < 3.2$
  - Hmx8 < 10
  - iso < 0.1
  - spatial track match (if required):
    * if matched track is type2: same as CC electrons. A type2 track points to calorimeter $|\eta_{\text{det}}| > 1.5$ and is covered by all CFT layers.
    * if matched track is type3: track match probability > 0.0, track $p_T > 10$ GeV, track fit $\chi^2 < 9.95$, at least two SMT hits and three CFT hits, beam-spot corrected DCA $|r_{\text{DCA}}| < 0.02$ cm. A type3 track is covered by at least two CFT layers.
    * if matched track is type4: track match probability > 0.0, track $p_T > 10$ GeV, track fit $\chi^2 < 9.95$, at least eight SMT hits, beam-spot corrected $|r_{DCA}| < 0.02$ cm, and $|\delta_{\text{trk}}| > 1.0$ where the track significance δ_{trk} is defined to describe the curvature of the track. A type4 track is covered by less than two CFT layers.

Events are further classified into CC-CC (both electrons are reconstructed in the CC), CC-EC (one electron is reconstructed in the CC, the other in the EC) and EC-EC (both electrons in the EC) categories. Event level selections are then applied:

- $|\text{vtxz}| < 40$ cm where vtxz is the z coordinate of the reconstructed primary vertex of the $p\bar{p}$ interaction.

- invariant mass of the di-lepton pair 60 GeV $< M_{ee} < 130$ GeV.

- instantaneous luminosity < 8.5.

- for CC-CC events, both electrons are required to have a spatial matched track. The two electrons are required to have opposite charge sign.

- for CC-EC events, only the CC electron is required to have a spatial matched track. The EC electron is supposed to have opposite charge sign.

- for EC-EC events, at least one electron is required to have a spatial matched track.

  - if both EC electrons have a matched track, the one with smaller type value is used to determine the charge, supposing the other electron has opposite charge.
  - if both EC electron tracks are the same type, the one with larger $|\delta_{\text{trk}}|$ is used to determine the charge, supposing the other electron has opposite charge.

4.3 Selected Z/γ^* candidates

After the above requirements, a total number of 560,267 events are selected, of which 248,380 are CC-CC events, 240,593 are CC-EC events and 71,294 are EC-EC events. The mass range is partitioned into different bins as 50-60 GeV, 60-70 GeV, 70-75 GeV, 75-81 GeV, 81-86.5 GeV, 86.5 - 89.5 GeV, 89.5-92 GeV, 92-97 GeV, 97-105 GeV, 105-115 GeV and 115-130 GeV. The bins widths were determined by the detector energy resolution. The slightly asymmetric bin widths around the Z pole is for reason that more events shift to the low mass side than to the high mass side.

The data sample is enlarged by 80% due to extension in phi-mod, η_{det} and other improvements. The details can be found in Tab. 4.4.

	increase (compared to the total number)
CC track-in-road*	15%
	10% in CC-CC, 5% in CC-EC
extending η_{det}	15%
	5% in CC-CC, 10% in CC-EC
EC-EC	20%
CC phi-mod	30%
	23% in CC-CC, 7% in CC-EC
loosening cuts**	6%
total	86%

Table 4.4: Increase of statistics in data. * CC track-in-road is an algorithm used in the data reprocessing [23]. ** We remove the cut of track isolation < 1.5 for EC electrons.

The invariant mass, $\cos\theta^*$, electron/positron p_T and detector η distributions of all selected RunIIb candidates are shown in Fig. 4.2 for CC-CC events, in Fig. 4.3 for CC-EC events and in Fig. 4.4 for EC-EC events.
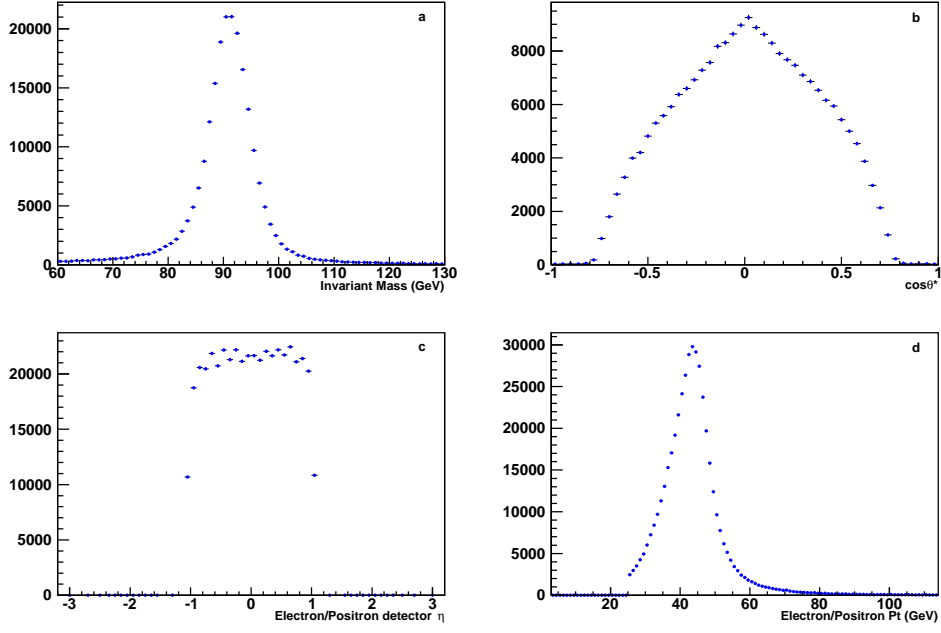
Figure 4.2: Distributions for CC-CC candidates in data (RunIIb). (*a*) Invariant *ee* mass; (*b*) $\cos\theta^*$; (*c*) electron/positron detector η; (*d*) electron/positron p_T.
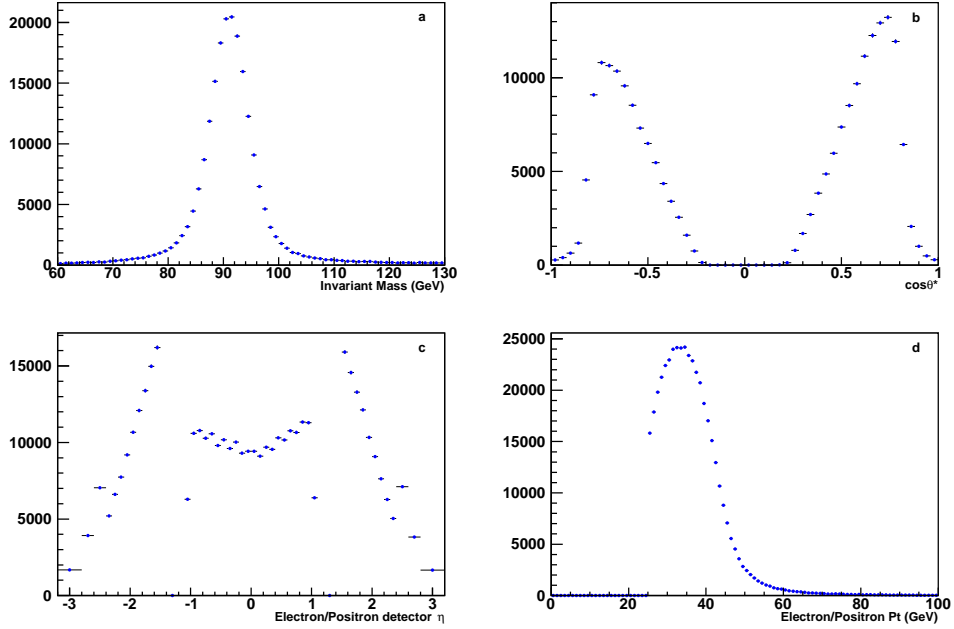
Figure 4.3: Distributions for CC-EC candidates in data (RunIIb). (*a*) Invariant *ee* mass; (*b*) $\cos\theta^*$; (*c*) electron/positron detector η; (*d*) electron/positron p_T.
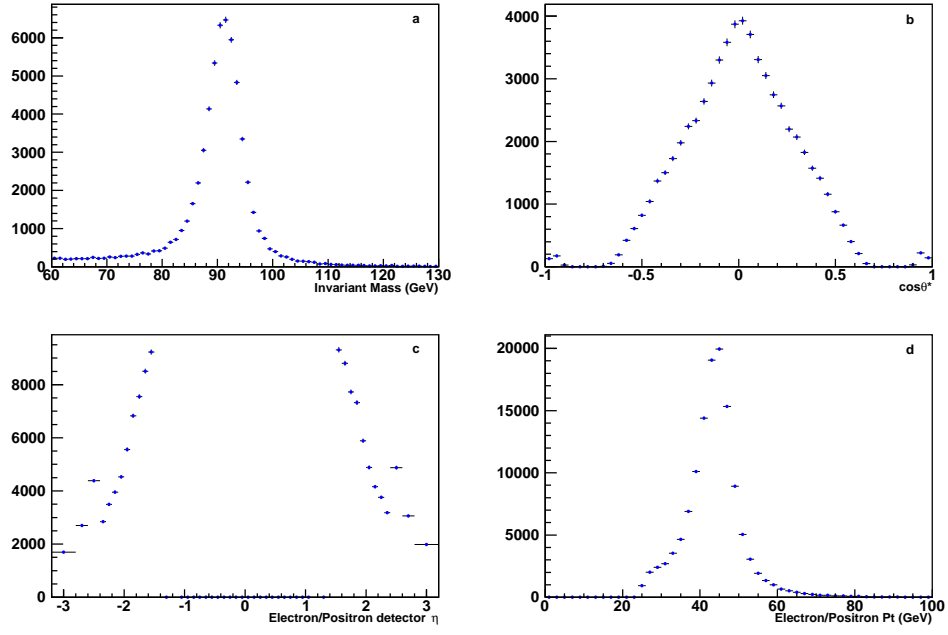
Figure 4.4: Distributions for EC-EC candidates in data (RunIIb). (*a*) Invariant *ee* mass; (*b*) $\cos\theta^*$; (*c*) electron/positron detector η; (*d*) electron/positron p_T.

Chapter 5

Electron Energy Calibration

5.1 Introduction

The electron energy measurement can be described by the difference D_E between the true energies and measured energies $D_E = E_{\text{true}} - E_{\text{meas}}$. The mean or peak value of the D_E distribution represents the scale of the energy measurement while the width describes the resolution. Note that no matter how large the resolution is, the energy measurement is considered to be statistically unbiased as long as the scale is close to 0. The scale does not have to be exactly a "scale" factor like

$$E_{\text{meas}} = \alpha \times E_{\text{true}}.$$

It can also be parameterized with other terms, such as

$$E_{\text{meas}} = \alpha \times E_{\text{true}} + \beta,$$

or with even higher order terms. Anything that effects the mean value of the measured energy should be absorbed in to the model of the energy scale. The change in the electron energy scale can cause shift in the peak of M_{ee} spectrum. To avoid any confusion, a "scale" factor meaning a ratio will be called as a "scaling" factor in this chapter.

The weak mixing angle, which is extracted from A_{FB} as a function of M_{ee}, depends strongly on the electron energy scale. Fig. 5.1 shows how A_{FB} distribution changes in the MC with different input $\sin^2 \theta_W$ values and electron energy scale. A slight change on the energy scale causes a shift on the entire distribution, which is same to that caused by a different $\sin^2 \theta_W$. Therefore, uncertainty due to energy scale determination is more significant than other sources. In the D0 5 fb^{-1} analysis, electron energy scale is the leading source of systematic uncertainty (except for PDF). In this thesis, more poorly measured electrons are included to have a larger data sample. Those electrons never had been used in any of the precious D0 precise measurements (like the W mass and asymmetry measurements). Therefore, it is critical to have a precise calibration on the electron energy scale.

This section will focus on a brief introduction to a new energy calibration method, followed by detailed discussions. The last section of this chapter is a summary.
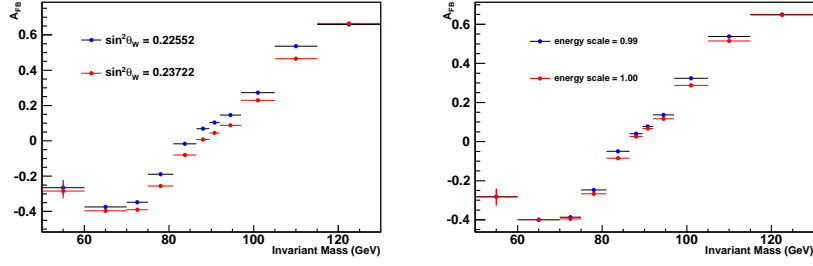
Figure 5.1: A_{FB} distributions in the MC with *left)* different input $\sin^2 \theta_W$ values and *right)* different energy scale. scale $= 1$ means the electron energy used in M_{ee} reconstruction and $\cos \theta^*$ calculation is exactly their true value; scale $= 0.99$ means the electron energy used is 1% lower than their true value.

5.1.1 Standard energy scale extraction and the new method

The Z boson mass reconstructed from dielectron in the final state can be expressed as:

$$M^2 = 2E_1 E_2 (1 - \cos \theta_{12}) \tag{5.1}$$

where E_1 and E_2 are the energy and θ_{12} is the opening angle between the directions of the two electrons. Thus it can be used to observe the electron energy scale. Usually, an overall scaling factor α is used to describe the energy scale, and applied to the MC simulations:

$$
\begin{aligned}
E_{\text{corr}} &= \alpha \times E \\
M_{\text{corr}}^2 &= 2 \times \alpha E_1 \times \alpha E_2 (1 - \cos \theta_{12}) \\
&= \alpha^2 \times M^2.
\end{aligned}
\tag{5.2}
$$

The scaling factor α is determined by comparing the mass distributions in data and MC, and requiring the best agreement between them. It works well when the energy measurement is not significantly biased so that a scaling factor is enough to describe the electron energy scale, and the determination of the scaling factor based on data-MC comparison is reasonable.

However, this method has great difficulties in this analysis. With poorly reconstructed electrons included this time, the energy measurement is significantly biased both in data and MC. This bias, which will be discussed in the following sections, has large dependence with η_{det} and instantaneous luminosity (L), causing up to $> 10\%$ deviation in energy measurement. Two major problems are raised. First, such a large and η_{det}-L dependent bias cannot be parameterized just into an overall scaling factor. More factors, like offsets are needed (introducing more factors needs rigorous studies to avoid over-many freedoms. It will be discussed in section 5.6). However, the correlations between multiple factors are serious obstacles in finding reasonable values of the calibration factors (that is why the poorly measured electrons were excluded). Second, the determination based on data-MC comparison is limited. In the standard method, this determination is using the M_{ee} from data as constraint to correct the MC simulations. However, the data itself also has large deviations. Even in the 5 fb^{-1} analysis that only high quality electrons were used, it still yielded large uncertainties due to background estimation, resolution, radiation and other effects.

A new energy calibration method is described in this chapter. The large deviation is modeled by multiple factors, including scaling factor (α) and offset factor (β). These factors are further required to be η_{det} and L dependent. To determine their values correctly, a technique is applied. This technique measures the correlations between scaling and offset factors before the determination. Instead of comparing the entire mass distributions in data and MC, the new method extract the peak of the M_{ee} spectrum. All factors are determined by requiring the peak to be consistent with the LEP measured Z boson mass, 91.1875 GeV. By doing this, data and MC can be separately calibrated.

To calibrate the data independently, the peak of M_{ee} spectrum is extracted and used instead of the entire mass distribution.

5.1.2 Strategy

The new energy calibration method is applied in the following strategy step by step:

- An instantaneous luminosity (L)-dependent scaling factor, α_L^{CC} (giving different correction values with L) is applied to the CC electrons. α_L^{CC} is determined by requiring the peak of M_{ee} in CC-CC events to be consistent with the LEP measured value in all instantaneous luminosity regions.

- An η_{det}-dependent scaling factor, α_η^{CC} (giving different correction values with η_{set}) is further applied to the CC electrons (α_L^{CC} has already been applied). α_η^{CC} is determined by requiring the peak of M_{ee} in CC-CC events to be consistent with the LEP measured value in all CC η_{det} regions.

- An L-dependent scaling factor, α_L^{EC}, is applied to the EC electrons. α_L^{EC} is determined by requiring the peak of M_{ee} in CC-EC events to be consistent with the LEP measured value in all instantaneous luminosity regions. Note that in this step the CC electrons have been corrected by α_L^{CC} and α_η^{CC}.

- An η_{det}-dependent scaling factor α_η^{EC} and an η_{det}-dependent offset factor β_η^{EC} are applied to the EC electrons. α_η^{EC} and β_η^{EC} are 100% correlated (which will be proved in the following sections). The correlation, or the relationship between β_η^{EC} and α_η^{EC} is measured using CC-EC events in all EC η_{det} regions.

- $beta_\eta^{EC}$ can be expressed by α_η^{EC} and the measured relationship. Then, their values are determined by requiring the peak of M_{ee} both in CC-EC and EC-EC events to be consistent with the LEP measured value, simultaneously.

This strategy is applied separately for the RunIIb1, 2, 3, 4 and RunIIa data and MC corresponding to different Tevatron run periods. Results of RunIIb2, which is the periods with largest bias in energy measurement, are chosen to be shown as examples to describe this method.

5.2 M_{ee} peak extraction and energy scale parameterization

To get the position of the M_{ee} peak, the spectrum is fitted by the following function:

$$
\begin{aligned}
N(m) &= G(m) \otimes L(m) + B(m) \\
G(m) &= \frac{1}{\sqrt{2\pi p_1}} \times e^{\frac{(m-p_0)^2}{2p_1^2}} \\
L(m) &= p_2 \frac{1}{2\pi} \frac{\Gamma_Z \cdot \frac{p_0}{M_Z}}{(m-p_0)^2 + \frac{(\Gamma_Z \cdot \frac{p_0}{M_Z})^2}{4}} \\
B(m) &= p_3 \cdot e^{p_4 \cdot (m-M_Z)} \cdot \int_{p_5(p_6-m)}^{\infty} e^{-t^2} dt
\end{aligned}
\tag{5.3}
$$

where m represents the dielectron invariant mass. $G(m) \otimes L(m)$ is the normalized Voigt function [24] used to describe the signal shape and $B(m)$ is used to describe the background. p_i are free parameters and p_0 represents the peak value of the M_{ee} spectrum. The statistical fluctuation of the M_{ee} spectrum is propagated into the fitting uncertainties. This function works well in extracting the peak when the background contribution is less than 5%.

The electron energy scale is parameterized and determined by observing M_{ee} peak. The parameterization and determination can be divided into four types:

- One electron Single parameter (O-S):
  This type is the simplest one, with only one free scaling parameter (α) applied on the energy of one of the electrons as:

$$
\begin{aligned}
E_{\text{corr}} &= \alpha \times E \\
M_{\text{corr}}^2 &= 2E_1(\alpha \cdot E_2)(1 - \cos\theta) \\
&= \alpha \times M^2.
\end{aligned}
$$

  Here E_1 is the energy of a tag electron which is considered to be well corrected. α can be well determined with only one mass constraint. It may be biased when α has some dependence, for example with η or instantaneous luminosity.

- Two electrons Single parameter (T-S):
  The dielectron mass in this case can be expressed as:

$$
\begin{aligned}
E_{\text{corr}} &= \alpha \times E \\
M_{\text{corr}}^2 &= 2(\alpha_1 \cdot E_1) \times (\alpha_2 \cdot E_2)(1 - \cos\theta) \\
&= \alpha_1 \alpha_2 \times M^2
\end{aligned}
$$

  where energies of both electrons need to be corrected. If $\alpha_1 = \alpha_2$, this situation is similar to the O-S case and one mass constraint is enough to determine it. If $\alpha_1 \neq \alpha_2$, for example α is η_{det}-dependent and the two electrons differ in their η, only one mass constraint is not perfect in the determination. However in some cases it may work with only one mass constraint when α_1 and α_2 are considered to be uncorrelated.

34

- One electron Multiple parameters (O-M):
  Additional parameters could be needed to accommodate the complexity of the energy modeling. For example, with an offset factor β, the dielectron mass in this situation can be expressed as:

$$
\begin{aligned}
E_{\text{corr}} &= \alpha \times E + \beta \\
M_{\text{corr}}^2 &= 2E_1 \cdot (\alpha \cdot E_2 + \beta)(1 - \cos\theta) \\
&= \alpha \cdot M^2 + 2E_1 \cdot \beta(1 - \cos\theta).
\end{aligned}
$$

The difference from the T-S type is that α_i for two electrons in the T-S type may be uncorrelated but α and β for the same electron must be strongly correlated. Therefore, at least two mass constraints are needed to determine the factors. Note that an M_{ee} spectrum often contains electrons in multiple η regions, so even more mass constraints have to be introduced when η-dependent α and β are involved.

- Two electrons Multiple parameters (T-M):
  This is even more complex than the O-M one:

$$
\begin{aligned}
E_{\text{corr}} &= \alpha \times E + \beta \\
M_{\text{corr}}^2 &= 2(\alpha_1 \cdot E_1 + \beta_1) \cdot (\alpha_2 \cdot E_2 + \beta_2)(1 - \cos\theta) \\
&= \alpha_1\alpha_2 \cdot M^2 \\
&\quad + 2(\alpha_1 E_1 \cdot \beta_2 + \alpha_2 E_2 \cdot \beta_1) \cdot (1 - \cos\theta) \\
&\quad + 2\beta_1\beta_2 \cdot (1 - \cos\theta).
\end{aligned}
$$

5.3 CC L-dependent correction

The energy measurement in the calorimeter is instantaneous luminosity L-dependent. In the MC simulations, it is dominated by the extra energy in the calorimeter due to additional $p\bar{p}$ interactions. In the data, it is dominated by the reduction in energy response due to the L_{inst}-dependent voltage drop which increased loading of the high voltage electrodes from increasing particle multiplicities with higher collision rates [25].

The CC L-dependent correction is a T-S correction with $\alpha_1 = \alpha_2$. An L-dependent scaling factor (α_L^{CC}) is applied to the CC electron energy:

$$
E_{\text{Lcorr}}^{CC} = \alpha_L^{CC} E^{CC}(L) \tag{5.4}
$$

where $E^{CC}(L)$ and E_{Lcorr}^{CC} are the electron energy before and after the correction. Using Eq. 5.4 and Eq. 5.1, the corrected mass M_{Lcorr}^{CC} can be described using α_L^{CC} and the mass before correction $M^{CC}(L)$:

$$
\begin{aligned}
(M_{\text{Lcorr}}^{CC})^2 &= 2[\alpha_L^{CC}]^2 \\
&\quad \times E_1^{CC}(L)E_2^{CC}(L)(1 - \cos\theta_{12}) \\
&= [\alpha_L^{CC}]^2[M^{CC}(L)]^2.
\end{aligned} \tag{5.5}
$$

In this case, the peak of M_{Lcorr}^{CC} is set to be the LEP measured value (91.1875 GeV). Then we have:

$$\alpha_L^{CC} = \frac{1}{M^{CC}(L)/91.1875}.$$

The value of $\alpha^{CC}(L_{\text{inst}})$ is determined by fitting $M^{CC}(L)/91.1875$ as a function of L. The function is in form of:

$$\frac{M^{CC}(L)}{91.1875} = \frac{1}{\alpha_L^{CC}} = p_0 - p_1 \times e^{p_3 \cdot L - p_2} \tag{5.6}$$

in the data and

$$\frac{M^{CC}(L)}{91.1875} = \frac{1}{\alpha_L^{CC}} = p_0 - p_1 \times L$$

in the MC. The fitting results are shown in Fig. 5.2. The L-dependence on M_{ee} peak before corrections is 1 GeV in data and 500 MeV in MC.
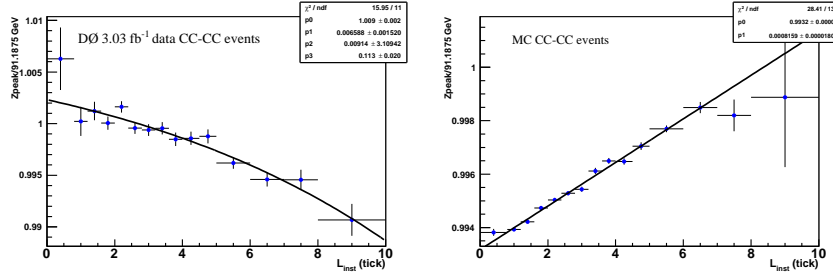
Figure 5.2: Fitting for $M^{CC}(L)/91.1875$ as a function of L in the data and MC.

5.4 CC η_{det}-dependent correction

The CC η_{det}-dependent correction is a T-S correction. It is performed by applying an η_{det}-dependent scaling factor (α_η^{CC}) to the CC electron energy. α_L^{CC} has been applied before this correction.

$$E_{\eta\text{corr}}^{CC} = \alpha_\eta^{CC} \times E^{CC}(\eta_{\text{det}}). \tag{5.7}$$

The values of α_η^{CC} is determined by looking for the minimal χ_{CC}^2 value which is defined as:

$$\chi_{CC}^2 \equiv \sum \frac{[M_{\eta_i\text{corr}}^{CC} - 91.1875]^2}{\sigma_{M_{\eta_i\text{corr}}^{CC}}^2} \tag{5.8}$$

where $M_{\eta_i\text{corr}}^{CC}$ is the fitted M_{ee} peak with α_η^{CC} applied. i marks a specific η_{det} region, and at least one of the electrons should be reconstructed in this region (no requirement on the other one) when using $M_{\eta_i\text{corr}}^{CC}$ to express the mass. $\sigma_{M_{\eta_i\text{corr}}^{CC}}$ is the corresponding uncertainty from M_{ee} peak extraction. The fitted value of α_η^{CC} in the data and MC are listed in Tab. 5.1.

η_{eta}	data scaling factors	MC scaling factors
-1.1 to -0.9	0.999066	0.994762
-0.9 to -0.7	0.998968	0.99941
-0.7 to -0.5	0.998931	1.00013
-0.5 to -0.3	1.00217	1.00135
-0.3 to 0.0	1.00143	1.00152
0.0 to 0.3	1.00026	1.00147
0.3 to 0.5	0.999768	1.00115
0.5 to 0.7	0.998966	1.00053
0.7 to 0.9	0.9981	0.998907
0.9 to 1.1	0.999649	0.994383

Table 5.1: α_η^{CC} in the data and MC.

Considering the η_{det}-dependence, there are 10 factors of α_η^{CC} fitted simultaneously. Values from this fitting are reasonable because enough mass constraints are used, and these factors, corresponding to different detector regions, are considered to be uncorrelated.

5.5 EC L-dependent correction

The EC L-dependent correction is applied by a scaling factor α_L^{EC}:

$$E_{\text{Lcorr}}^{EC} = \alpha_L^{EC} \times E^{EC}(L). \tag{5.9}$$

The M_{ee} spectrum in CC-EC events is used in the determination of α_L^{EC}. The CC electrons are corrected by α_L^{CC} and α_η^{CC}, thus only the EC electrons contribute to the L-dependence:

$$
\begin{aligned}
(M_{\text{Lcorr}}^{CE})^2 &= 2E_{\text{fullcorr}}^{CC} \times E_{\text{Lcorr}}^{EC}(1 - \cos\theta_{12}) \\
&= 2E_{\text{fullcorr}}^{CC} \times \\
&\quad \alpha_L^{EC} \cdot E^{EC}(L)(1 - \cos\theta_{12}) \\
&= \alpha_L^{EC}[M^{CE}(L)]^2.
\end{aligned} \tag{5.10}
$$

Hence for CC-EC events, it is an O-S type. α_L^{EC} can be determined by fitting $M^{CE}(L)/91.1875$ similar to the α_L^{CC} determination. The fitting function used for EC electrons is

$$\frac{M^{CE}(L)}{91.1875} = \sqrt{\frac{1}{\alpha_L^{EC}}} = p_0 + p_1 \cdot e^{-L}$$

in the data and

$$\frac{M^{CE}(L)}{91.1875} = \sqrt{\frac{1}{\alpha_L^{EC}}} = p_0 - p_1 \cdot e^{-p_3 \cdot L - p_2}$$

in the MC. The fitting results are shown in Fig. 5.3. The L-dependence on M_{ee} peak before corrections is about 500 MeV.

37
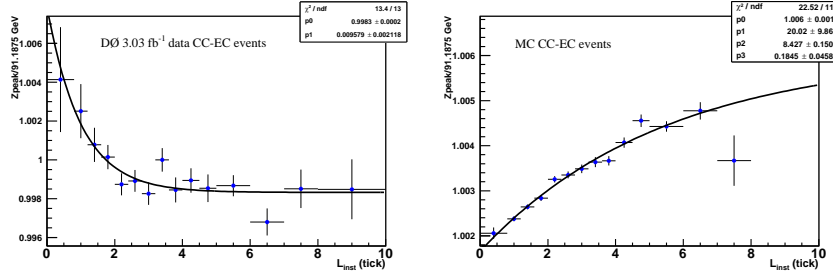
Figure 5.3: Fit for $M^{CE}(L)/91.1875$ as a function of L in the data and MC.

5.6 EC η_{det}-dependent correction

The EC η_{det}-dependent correction is further applied after the EC L-dependent correction. Generally, an η_{det}-dependent scaling factor α_η^{EC} and an η_{det}-dependent offset factor β_η^{EC} are used. α_η^{EC} and β_η^{EC} are strongly correlated. First, the correlation between them are measured using CC-EC events. Then, their values are determined using M_{ee} peaks in both CC-EC and EC-EC events. All the corrections described in the previous sections are already applied.

5.6.1 Correction function

The number of free factors used in the correction function should be carefully studied. The more factors we use, the more mass constraints need to be introduced. More importantly, when unnecessary factors are used which means there is no such effect in the energy measurement related to the factors, the calibration becomes just a mathematical trick. (People have introduced an extra higher order term of $\gamma \times E^2$ to cover the problem caused by correlations instead of detailed study. This is "unnecessary" because study from previous calibrations indicates that the calorimeter keeps a linear response in a large range of energy. Even if this higher order term helps in achieving agreement in some specific mass spectrum, it is not really calibrating the electron energy. Electron energy with such term may be even more biased.) Therefore, we have to provide reasonable explanation of introducing β_η^{EC}.

If the EC η_{det}-dependence can be described with a scaling factor (α_L^{EC}) only, as

$$E_{\eta\text{corr}}^{EC} = \alpha_\eta^{EC} \times E^{EC}(\eta_{\text{det}}),$$

then, it is an O-S correction for CC-EC events and T-S correction for EC-EC events:

$$
\begin{aligned}
(M_{\eta\text{corr}}^{CE})^2 &= 2E_{\text{fullcorr}}^{CC} \\
&\quad \times \alpha_\eta^{EC} \cdot E^{EC}(\eta_{\text{det}})(1 - \cos\theta_{12}) \\
&= \alpha_\eta^{EC} \cdot [M^{CE}(\eta_{\text{det}})]^2 \qquad (5.11) \\
(M_{\eta\text{corr}}^{EE})^2 &= 2\alpha_{\eta_1}^{EC} \cdot E^{EC}(\eta_{1\text{det}}) \\
&\quad \times \alpha_{\eta_2}^{EC} \cdot E^{EC}(\eta_{2\text{det}}) \cdot (1 - \cos\theta_{12}) \\
&= \alpha_{\eta_1}^{EC} \alpha_{\eta_2}^{EC} \cdot [M^{EE}(\eta_{1\text{det}}, \eta_{2\text{det}})]^2. \qquad (5.12)
\end{aligned}
$$

38

M^{CE} is $\mathcal{O}(\alpha_\eta^{EC})$ diverging from its true value while M^{EE} is $\mathcal{O}([\alpha_\eta^{EC}]^2)$ diverging from its true value. Therefore, the η_{det}-dependence of M^{EE} is expected to be larger than that of M^{CE}.

If an offset β_η^{EC} is necessary in the energy modeling:

$$E_{\eta\text{corr}}^{EC} = \alpha_\eta^{EC} \times E^{EC}(\eta_{\text{det}}) + \beta_\eta^{EC}, \tag{5.13}$$

then, it is an O-M correction for CC-EC events and T-M correction for EC-EC events:

$$
\begin{aligned}
(M_{\eta\text{corr}}^{CE})^2 &= 2E_{\text{fullcorr}}^{CC} \cdot [\alpha_\eta^{EC} \cdot E^{EC}(\eta_{\text{det}}) + \beta_\eta^{EC}] \times (1 - \cos\theta_{12}) \\
&= \alpha_\eta^{EC} \cdot [M^{CE}(\eta_{\text{det}})]^2 \\
&\quad + 2E_{\text{fullcorr}}^{CC} \cdot \beta_\eta^{EC} \cdot (1 - \cos\theta_{12}) \\
(M_{\eta\text{corr}}^{EE})^2 &= 2[\alpha_{\eta 1}^{EC} \cdot E^{EC}(\eta_{1\text{det}}) + \beta_{\eta 1}^{EC}] \\
&\quad \times [\alpha_{\eta 2}^{EC} \cdot E^{EC}(\eta_{2\text{det}}) + \beta_{\eta 2}^{EC}] \cdot (1 - \cos\theta_{12}) \\
&= \alpha_{\eta 1}^{EC} \cdot \alpha_{\eta 2}^{EC} \cdot [M^{EE}(\eta_{1\text{det}}, \eta_{2\text{det}})]^2 \\
&\quad + 2[\alpha_{\eta 1}^{EC} \cdot \beta_{\eta 2}^{EC} \cdot E^{EC}(\eta_{1\text{det}}) \\
&\quad + \alpha_{\eta 2}^{EC} \cdot \beta_{\eta 1}^{EC} \cdot E^{EC}(\eta_{2\text{det}})] \cdot (1 - \cos\theta_{12}) \\
&\quad + 2\beta_{\eta 1}^{EC}\beta_{\eta 2}^{EC} \cdot (1 - \cos\theta_{12}).
\end{aligned}
\tag{5.14}
$$

In this case, the dependence in M_{ee} is dominated by the coefficient $(1 - \cos\theta_{12})$ because the energy E associated with $(1 - \cos\theta_{12})$ is very large (hundreds of GeV). The directions of the two electrons in EC-EC events are close to each other due to a heavy boost of the Z boson at TeV hadron collider experiments, which results in small opening angle θ_{12}, as shown in Fig. 5.4. Therefore, the η_{det}-dependence of M^{CE} is expected to be larger than that of M^{EE}.
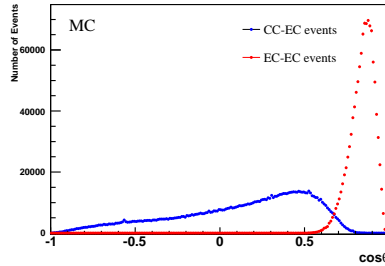
Figure 5.4: $\cos\theta_{12}$ distributions in CC-EC and EC-EC events.

The peaks of M^{CE} and M^{EE} spectrums as a function of η_{det} observed in data and MC are shown in Fig. 5.5. The larger deviation in CC-EC events indicates that an offset factor is necessary in the correction function Eq. 5.13.
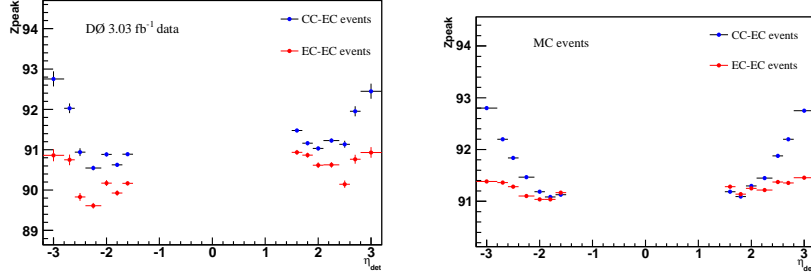
Figure 5.5: The peaks of M^{CE} and M^{EE} spectrums as a function of η_{det} in CC-EC and EC-EC events. For CC-EC events, η_{det} means the EC electron should be reconstructed in that region. For EC-EC events, η_{det} means at least one of the electrons should be reconstructed in that region (no requirement on the other one).

5.6.2 β-α relationship

Eq. 5.13 has two factors β_η^{EC} and α_η^{EC}, and they are correlated. The correlation can be reduced by measuring the relationship between them. The mass of CC-EC events given in Eq 5.14 can also be expressed as

$$
\begin{aligned}
(M_{\eta\text{corr}}^{CE})^2 &= \alpha_\eta^{EC} \cdot \left[M^{CE}(\eta_{\text{det}}) \right]^2 \\
&+ 2E_{\text{fullcorr}}^{CC} \cdot \beta_\eta^{EC} \cdot (1 - \cos\theta_{12}) \\
&= \alpha_\eta^{EC} \cdot \left[M^{CE}(\eta_{\text{det}}) \right] \\
&+ \left[M^{CE}(\eta_{\text{det}}) \right]^2 \cdot \beta_\eta^{EC} \cdot \frac{1}{E^{EC}(\eta_{\text{det}})},
\end{aligned}
$$

and thus

$$
\begin{aligned}
\beta_\eta^{EC} &= E^{EC}(\eta_{\text{det}}) \cdot \alpha_\eta^{EC} \\
&+ \frac{(M_{\eta\text{corr}}^{CE})^2}{[M^{CE}(\eta_{\text{det}})]^2} \cdot E^{EC}(\eta_{\text{det}})
\end{aligned} \tag{5.15}
$$

For the CC-EC events with the EC electrons reconstructed in a specific η_{det} region, β_η^{EC} and α_η^{EC} are considered to be constants. Their relationship can be derived by expressing the mathematical expectation of Eq. 5.15:

$$
\begin{aligned}
\beta_\eta^{EC} &= A(\eta_{\text{det}}) \cdot \alpha_\eta^{EC} + B(\eta_{\text{det}}) \tag{5.16} \\
A(\eta_{\text{det}}) &= -\mathcal{E}[E^{EC}(\eta_{\text{det}})] \\
B(\eta_{\text{det}}) &= \mathcal{E}\left[\frac{(M_{\eta\text{corr}}^{CE})^2}{[M^{CE}(\eta_{\text{det}})]^2} \cdot E^{EC}(\eta_{\text{det}}) \right],
\end{aligned}
$$

where $\mathcal{E}$ means mathematical expectation. Practically, $A(\eta_{\text{det}})$ and $B(\eta_{\text{det}})$, which depend on the kinematic distributions of E^{EC} and $\cos\theta_{12}$ of the CC-EC events, can be measured by the following steps:

- Fix α_η^{EC} to a given value α_i.

- Fit for the value of β_η^{EC} (β_i) by requiring the peak of $M_{\eta\text{corr}}^{CE}$ after correction to be consistent with 91.1875 GeV.

- Repeat above two steps with different fixed α_η^{EC} value.

- Fit for $A(\eta_{\text{det}})$ and $B(\eta_{\text{det}})$ using all (α_i, β_i) pairs.

Fig. 5.6 shows an example of β-α fitting in the region $-2.6 < |\eta_{\text{det}}| < -2.4$. The measured values of $A(\eta_{\text{det}})$ and $B(\eta_{\text{det}})$ in data and MC are listed in Tab. 5.2. With measured $A(\eta_{\text{det}})$ and $B(\eta_{\text{det}})$, one degree of freedom in Eq. 5.13 is removed. The correction function can be rewritten as

$$E_{\eta\text{corr}}^{EC} = \alpha_\eta^{EC} \times E^{EC}(\eta_{\text{det}}) + \beta_\eta^{EC}(\alpha_\eta^{EC}). \tag{5.17}$$
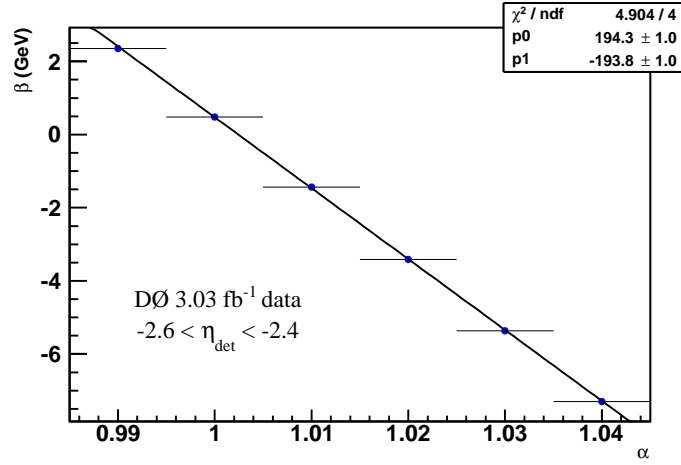
Figure 5.6: β-α fitting in the region $-2.6 < |\eta_{\text{det}}| < -2.4$ in data. Each point in the plot represents an α-β pair.

η_{det}	$A(\eta_{\text{det}})$ in data	$B(\eta_{\text{det}})$ in data	$A(\eta_{\text{det}})$ in MC	$B(\eta_{\text{det}})$ in MC
-3.2 to -2.8	-291.638	281.061	-270.775	262.533
-2.8 to -2.6	-232.658	227.547	-225.237	220.953
-2.6 to -2.4	-193.829	194.34	-190.077	188.114
-2.4 to -2.3	-174.151	174.915	-169.013	168.116
-2.3 to -2.2	-158.247	161.904	-157.285	156.682
-2.2 to -2.1	-146.957	147.785	-145.223	145.059
-2.1 to -2.0	-136.674	136.374	-134.361	134.532
-2.0 to -1.9	-126.487	127.56	-123.901	124.426
-1.9 to -1.8	-114.556	116.13	-114.208	114.848
-1.8 to -1.7	-107.35	107.912	-105.415	106.086
-1.7 to -1.6	-99.6225	99.807	-97.8592	98.4614
-1.6 to -1.5	-91.4833	91.8785	-90.6525	90.9248
1.5 to 1.6	-90.4498	89.6821	-89.6258	89.6758
1.6 to 1.7	-99.342	98.2954	-96.6541	97.2002
1.7 to 1.8	-105.928	105.47	-104.211	104.802
1.8 to 1.9	-114.205	114.181	-112.611	113.245
1.9 to 2.0	-123.797	124.273	-122.346	122.25
2.0 to 2.1	-135.684	135.355	-132.123	132.449
2.1 to 2.2	-144.44	144.722	-142.977	142.865
2.2 to 2.3	-155.836	156.247	-154.218	153.9
2.3 to 2.4	-173.82	171.17	-167.227	166.433
2.4 to 2.6	-189.889	189.566	-186.652	184.607
2.6 to 2.8	-225.968	221.85	-220.777	216.822
2.8 to 3.2	-288.994	280.801	-264.699	257.132

Table 5.2: Measured values of $A(\eta_{\text{det}})$ and $B(\eta_{\text{det}})$ in data and MC.

5.6.3 Determination of α_η^{EC} and β_η^{EC}

Now, any possible values of α_η^{EC} and β_η^{EC} that satisfy the relationship in Eq. 5.16 can correct the peak of the M^{CE} spectrum in the corresponding η_{det} region. However, only one β_η^{EC} and α_η^{EC} pair is the physical one that represents the real energy modeling, and thus can simultaneously correct the peak of the M^{CE} and M^{EE} spectrums. The values of α_η^{EC} are determined by looking for the minimal value of χ^2_{EC} which is defined as:

$$\chi^2_{EC} \equiv \sum \frac{[M^{CE}_{\eta_i\text{corr}} - 91.1875]^2}{\sigma^2_{M^{CE}_{\eta_i\text{corr}}}}$$
$$+ \sum \frac{[M^{EE}_{\eta_i\text{corr}} - 91.1875]^2}{\sigma^2_{M^{EE}_{\eta_i\text{corr}}}} \tag{5.18}$$

where the peaks of dielectron mass both in CC-EC and EC-EC events are considered. The values of α_η^{EC} are listed in Tab. 5.3. The values of β_η^{EC} can be calculated from Eq. 5.16.

η_{det}	$\alpha(\eta_{\mathrm{det}})$ in data	$\alpha(\eta_{\mathrm{det}})$ in MC
-3.2 to -2.8	1.09866	1.0993
-2.8 to -2.6	1.03602	1.06219
-2.6 to -2.4	1.03604	1.04165
-2.4 to -2.1	1.03278	1.03356
-2.1 to -1.9	1.00527	1.02619
-1.9 to -1.7	1.03131	1.02594
-1.7 to -1.5	1.01784	1.0285
1.5 to 1.7	1.02357	1.03383
1.7 to 1.9	0.991413	1.02672
1.9 to 2.1	1.01575	1.02112
2.1 to 2.4	1.02588	1.03056
2.4 to 2.6	1.06403	1.03806
2.6 to 2.8	1.06074	1.05664
2.8 to 3.2	1.08394	1.09688

Table 5.3: Fitted values of $\alpha^{EC}(\eta_{\mathrm{det}})$ in data and MC.

5.7 Results

After all corrections applied, the peak of $M_{\mathrm{fullcorr}}^{CC}$, $M_{\mathrm{fullcorr}}^{CE}$ and $M_{\mathrm{fullcorr}}^{EE}$ as a function of L and η_{det} in data and MC are shown in Fig. 5.7 to Fig. 5.10. The dependence with L after correction is negligible. The dependence with η_{det} is reduced from larger than 2 GeV to less than 100 MeV in data and 10 MeV in MC.

The calibration depends only on L and η_{det}. Electrons in the same L and η_{det} configuration are corrected by exactly the same functions and factors. The peaks of M_{ee} spectrums in CC-CC, CC-EC and EC-EC categories can be calibrated simultaneously.

Figure 5.7: $M_{\mathrm{fullcorr}}^{CC}/91.1875$ as a function of L in data and MC after the L-dependent correction.

43
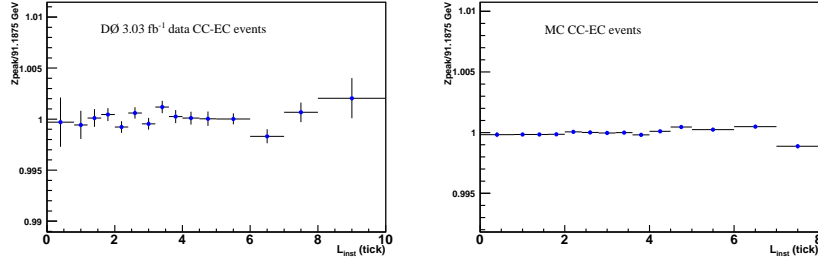
Figure 5.8: $M_{\mathrm{fullcorr}}^{CE}/91.1875$ as a function of L in data and MC after the L-dependent correction.
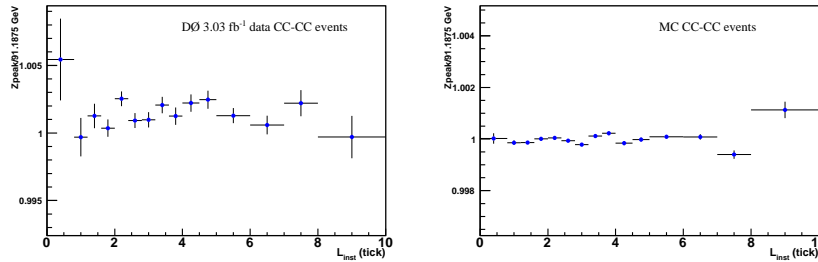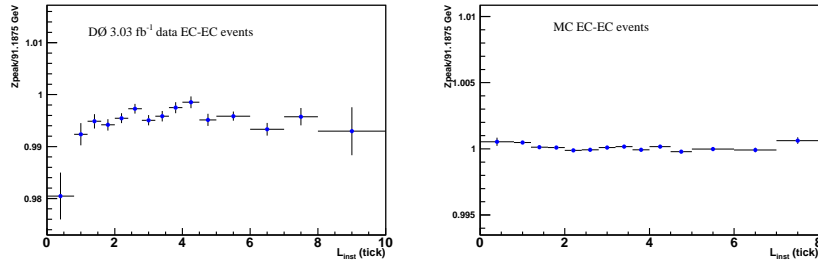

Figure 5.9: $M_{\mathrm{fullcorr}}^{EE}/91.1875$ as a function of L in data and MC after the L-dependent correction.
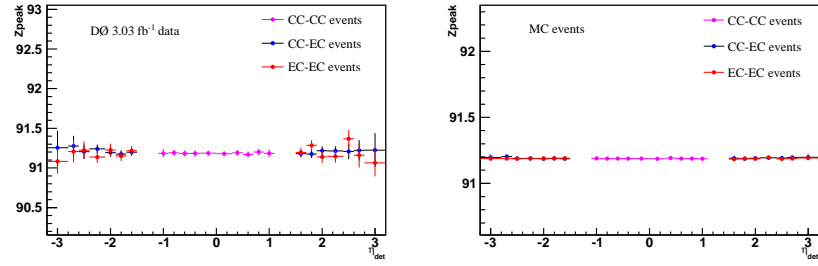
Figure 5.10: $M_{\mathrm{fullcorr}}^{CC}$, $M_{\mathrm{fullcorr}}^{CE}$ and $M_{\mathrm{fullcorr}}^{EE}$ as a function of η_{det} after calibration in data and MC.

5.8 Further tests

5.8.1 Test on EOP

In this method, the L-dependent correction factor is determined by observing the peak of M_{ee} as a function of L. It can be determined by another observable which is defined as EOP:

$$\text{EOP} \equiv \frac{E_{\text{cal}}^{T}}{p_{\text{trk}}^{T}}$$

where E_{cal}^{T} is the transverse energy of electrons measured in the calorimeter and p_{trk}^{T} is the transverse momentum of electrons measured in the tracking system. p_{trk}^{T} is not sensitive to L. Hence the correction factor α_{L}^{CC} in the CC can be determined by fitting the EOP as a function of L [20]:

$$\begin{aligned} \alpha_{L}^{CC} &\propto \text{EOP}(L) \\ &= \frac{1}{k_0 + k_1 \cdot L}. \end{aligned}$$

The fitting of α_{L}^{CC} from M_{ee} peak can also be achieved with a linear function instead of Eq. 5.6:

$$\begin{aligned} \alpha_{L}^{CC} &\propto \frac{91.1875}{M^{CC}(L)} \\ &= \frac{1}{p_0 + p_1 \cdot L}. \end{aligned}$$

The fitted p_1 and k_1 in data and MC are listed in Tab. 5.4 and compared to the results from the EOP method. These two methods give consistent results within statistical uncertainties. This test indicates that the extraction of M_{ee} peak and further determination on calibration factors using that peak are reasonable.

We do not use the EOP method because it has difficulties in the EC region due to a low track match efficiency and poor reconstruction quality.

	k_1 from EOP	p_1 from Z-peak
data	0.00124±0.0001	0.000123±0.0001
MC	0.0008120±0.000018	0.0008122±0.000017

Table 5.4: The CC L-dependent correction factor determined from the EOP method and M_{ee} peak method.

5.8.2 Test on $A(\eta_{\text{det}})$ and $B(\eta_{\text{det}})$

The values of $A(\eta_{\text{det}})$ and $B(\eta_{\text{det}})$ are measured using M^{CE} in CC-EC events. Eq. 5.16 shows that the absolute value of $A(\eta_{\text{det}})$ equals to the average of the observed electron energy in the given η_{det} region, and $B(\eta_{\text{det}})$ is close to $|A(\eta_{\text{det}})|$ but with an opposite sign. The comparison between the measured $|A(\eta_{\text{det}})|$, $B(\eta_{\text{det}})$ as a function of η_{det} are compared to the observed

average E. The comparison is shown in Fig. 5.11. They measured $A(\eta_\text{det})$ and $B(\eta_\text{det})$ are consistent with what have been predicted by Eq. 5.16 predicted.
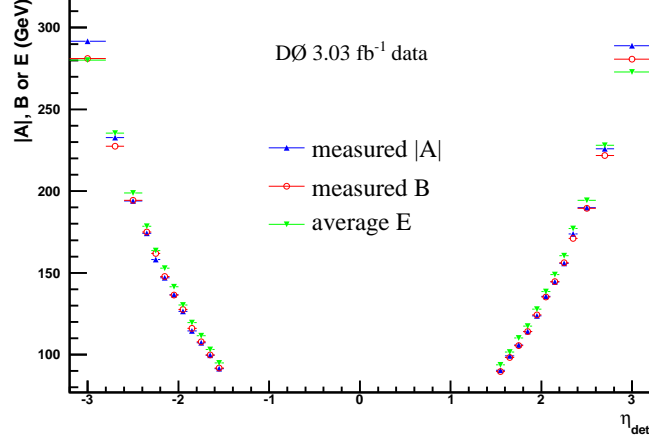
Figure 5.11: Measured $|A(\eta_\text{det})|$ and $B(\eta_\text{det})$, and the observed average energy E in data.

5.8.3 Test on MC truth level information

The relative difference in energy in the MC is used to test whether the method calibrates the energy of electrons. The relative difference is defined as:

$$R = \frac{E_\text{reco} - E_\text{truth}}{E_\text{truth}} \tag{5.19}$$

where E_reco is the reconstruction level energy and E_truth is the generator level energy. The distributions of R before and after energy calibration are shown in Fig. 5.12. The mean of the distribution before calibration is $0.013 \pm 5 \times 10^5$. After calibration, it is reduced to 0.0002. This test indicates that the calibration method is calibrating electron energy, which is more than just changing the shape of M_{ee} spectrum.
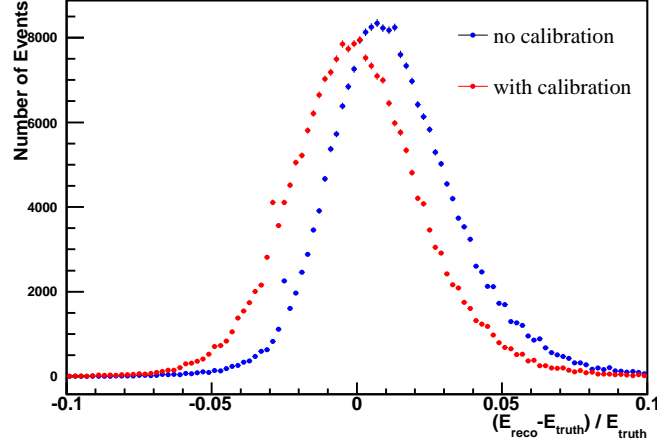
Figure 5.12: R before and after energy calibration.

5.8.4 Test on extra-offset

To estimate the inaccuracy on the entire calibration, including the measurement of β-α relationship and the determination of α_η^{CC} and α_η^{EC}, the fitting described in Eq. 5.18 and Eq. 5.8 is performed again with an extra new offset δ_η:

$$E_{\eta\mathrm{corr}}^{CC} = \alpha_\eta^{CC} \times E^{CC}(\eta_{\mathrm{det}}) + \delta_\eta^{CC} \tag{5.20}$$

$$\begin{aligned} E_{\eta\mathrm{corr}}^{EC} &= \alpha_\eta^{EC} \times E^{EC}(\eta_{\mathrm{det}}) + \beta_\eta^{EC}(\alpha_\eta^{EC}) \\ &\quad + \delta_\eta^{EC}) \end{aligned} \tag{5.21}$$

where δ_η is an additional offset. $A(\eta_{\mathrm{det}})$ and $B(\eta_{\mathrm{det}})$, together with the β-α relationship are fixed as their measured values. In this test, δ_η and α_η^{CC} or α_η^{EC} are fitted simultaneously. The values of δ_η as a function of η_{det} in data and MC are shown in Fig. 5.13. The average value of δ_η is around 10 MeV which is negligible with respect to the electron energy (greater than 100 GeV).

47
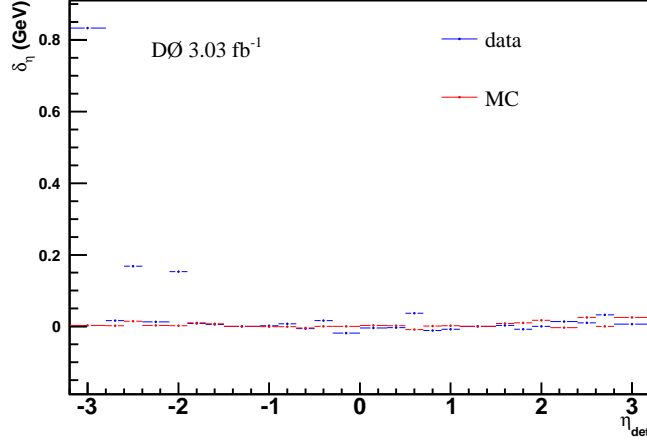
Figure 5.13: δ_η in data and MC as a function of η.

5.9 Conclusion

This chapter describes a new energy calibration method. It provides precise energy calibrations to both data and MC thus is the basis on which the analysis can use those never-been-used electrons. In another word, both statistical and systematic uncertainties of the whole analysis are reduced by this calibration.

The success of this calibration comes from several improves compared to the old standard method:

- a technique is developed to measure the correlations between factors, so that offset factors can be used in addition to scaling factors. With scaling and offset factors, the large deviation is well modeled.

- all factors are determined by observing the M_{ee} peak instead of the entire mass spectrum, so that data and MC can be independently calibrated. Besides, when η_{set} and L dependence are introduced to factors, the determination using M_{ee} peak can suppress uncertainties due to backgrounds, resolution, radiation and other effects.

- the only physics constraint used in this calibration is the LEP measured Z boson mass. No further information of the detector itself is needed.

After all the corrections, the dependence with instantaneous luminosity is negligible. The dependence with η_{det} is reduced from >2 GeV to 100 MeV in data and 10 MeV in MC. The calibration is crucial to this analysis because energy scale is the dominant systematic uncertainty due to a same effect on the A_{FB} compared to that from a different $\sin^2 \theta_W$ value.

Chapter 6

Other Corrections to MC

6.1 Introduction

Several corrections and reweightings are applied to the MC after the energy calibration. The electron energy resolution is discussed in section 6.2. It is much less significant to this analysis because it does not change the average value of A_{FB}.

Section 6.3 describes the determination of electron selection efficiencies in data and MC. Relative scale factors are derived and applied to the simulation to correct the MC to data. Electron selection efficiencies are divided into three steps: pre-selection (ID, emf, isolation cuts), EMID (Hmx cut) and track matching efficiency. The efficiencies correction is less significant to the weak mixing angle measurement because they cancel out in the A_{FB} defined as a ratio between numbers of the forward and backward events.

Other reweightings to MC are described in Section 6.4, including the instantaneous luminosity reweighting, the vertex z smearing and other high order corrections to the generator level information. These corrections help the MC simulations describe the data better. But systematic uncertainties on the A_{FB} and the weak mixing angle due to these corrections are negligible.

Finally, the charge mis-identification probability is measured. The probability measured in the MC is scaled to match that in the data. Details are discussed in section 6.5. The charge measurement is crucial. But uncertainties from this part is small because the charge mis-identification probability is negligible.

6.2 Energy resolution

After the energy calibration, the absolute scale of electron energy has been corrected by comparing the M_{ee} peak to the LEP measured Z boson mass as a function of instantaneous luminosity and η_{det}. However, the MC simulations still predict different resolution of electron energy measurement from that in the data. The resolution can be studied by observing the width in the M_{ee} spectrums. Thus additional electron energy resolution smearing needs to be developed and applied to the MC.

For the EC electrons and CC phi-mod center electrons, the resolution smearing is done by using the following formula:

$$E^{\text{smear}} = E \times (1 + c \times x) \tag{6.1}$$

where $E^{\text{smear}}(E)$ are the energy after(before) smearing. The coefficient c is the energy smearing parameter, and x is a random number generated from a nominal Gaussian distribution with mean of zero and sigma of one. Note that there is no further global scale factors in the smearing function. For the CC phi-mod boundary electrons, the smearing is done with a CrystalBall function:

$$E^{\text{smear}} = E \times a \times (1.0 + CB(x; \alpha, n, M, \sigma)) \tag{6.2}$$

where $CB(x; \alpha, n, M, \sigma)$ is a CrystalBall function defined as

$$CB(x; \alpha, n, M, \sigma) = N \times e^{-\frac{(x-M)^2}{2\sigma^2}} \tag{6.3}$$

where N is a normalization factor, n is fixed to be 7.0 and α is fixed to be 0. A reminder: the phi-mod boundary electrons are those reconstructed near the boundaries of the calorimeter modules in the ϕ direction. These electrons were previous ignored due to their poor energy measurement.

The smear factors are determined by requiring the best agreement in M_{ee} spectrum between data and MC in a range of $60 < M_{ee} < 130$ GeV. The procedure is done in the following steps successively:

- The CC gaussian smear factor is tuned using the CC-CC events of which both electrons phi-mod center.

- The CC CrystalBall smear factor is tuned using all CC-CC events, of which the phi-mod center electrons are already smeared by the CC gaussian factor.

- The EC Gaussian smear factor is tuned using the CC-EC events, of which the CC electrons must be reconstructed as phi-mod center.

The Gaussian smear factor is found to be 0.02448 ± 0.00003 for the CC phi-mod center electrons and 0.02533 ± 0.00003 for the EC electrons. The CrystalBall smear factors are found to be $a = 0.99817 \pm 0.00015$, $M = 0.00024 \pm 0.00006$ and $\sigma = 0.908532 \pm 0.000004$.

6.3 Electron efficiencies

6.3.1 Tag-and-Probe method

The standard Tag-and-Probe method [26] is applied to the data and MC samples: an electron candidate passing requirements tighter than the offline selection cuts is set as a tag electron, the probe electron is selected by requiring $75 < M_{ee} < 105$ GeV. Probe electrons or tracks form a minimally biased electron sample with high purity and are optimal for studying the selection efficiencies. The requirements for the tag electron are as follow:

- the EM object must be in the CC η-fiducial and ϕ-fiducial region;

- transverse energy $E_T > 25$ GeV;

- ID $= \pm 11$, iso < 0.10, emf > 0.95, HMx7 < 12;

- has a high quality matched track with track $p_T > 25$ GeV, track $r_{\text{dca}} < 0.2$ cm, $\chi^2/\text{ndof} < 5$, nCFT $>= 9$ and nSMT$>= 2$.

6.3.2 Electron pre-selection efficiency

The electron pre-selection includes cuts on particle ID, iso and emf. To obtain a probe electron, a track opposite to the tag electron is selected with

- track $p_T > 20$ GeV, $r_{dca} < 0.02$ cm and $\chi^2/ndof < 5$;

- if type 1 or type 2 track: nCFT $>= 9$ and nSMT$>= 2$;

- if type 3 track: nCFT $>= 3$ and nSMT$>= 2$;

- if type 4 track: nSMT $>= 8$ and $|track\ significance| >= 1.0$;

- opposite charge with the tag electron;

- $\Delta\phi(tag\ track,\ test\ track) > 2$;

- $70 < M(tag\ electron,\ test\ track) < 110$ GeV.

If the extrapolated position of the test track in the third layer of the calorimeter (EM3) is in the detector geometry coverage, then it would be taken as the denominator for the pre-selection efficiency study. The extrapolated track is required to be phi-mod center in the calorimeter for the phi-mod center efficiency measurement, and to be phi-mod boundary for the phi-mod boundary efficiency measurement.

The denominator identified test track is then matched with an EM cluster in $\Delta R < 0.14$ to get the probe EM cluster. Probe EM clusters that satisfy the following calorimeter based requirements are taken as the numerator of the pre-selection efficiency:

- ID $= 10, \pm 11$, emf > 0.9, iso $< 0.15(\text{CC})$ or $0.10(\text{EC})$;

- $E_T > 25$ GeV;

- $70 < M(\text{tag electron}, \text{probe electron}) < 110$ GeV.

The efficiencies measured as a function of detector η are shown in Fig. 6.1 for data and MC respectively. The data/MC ratios, as shown in Fig. 6.2, would be applied onto MC electrons in simulation, and the statistics fluctuation of the ratios in each η bin would be taken as systematics uncertainty of pre-selection.

Figure 6.1: Pre-selection efficiency as a function of detector η for RunIIb data and MC. (*a*) CC phi-mod center electrons; (*b*) CC phi-mod boundary electrons; (*c*) EC electrons.
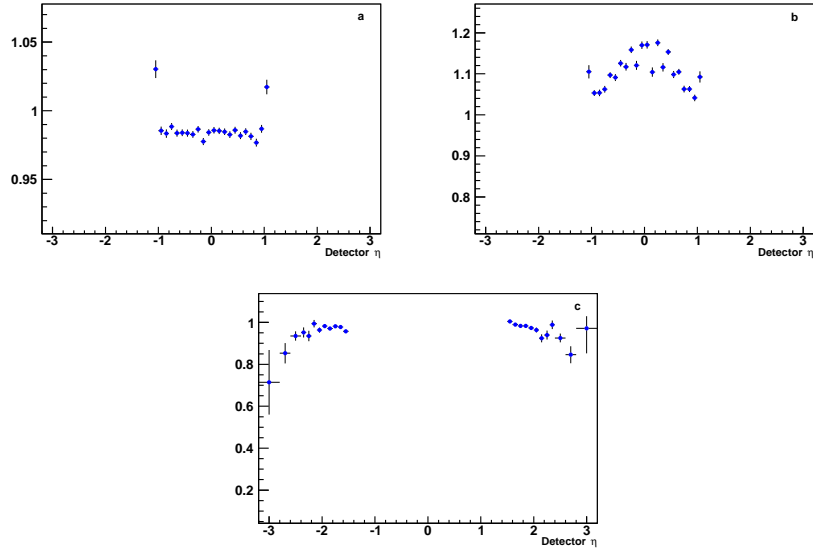
Figure 6.2: The data/MC ratio of pre-selection efficiency as a function of detector η for RunIIb data and MC. (*a*) CC phi-mod center electrons; (*b*) CC phi-mod boundary electrons; (*c*) EC electrons.

6.3.3 Electron ID efficiency

Based on pre-selection, the electron ID efficiencies, namely Hmx7 for CC electrons and Hmx8 for EC electrons, can be determined. The probe EM cluster is selected with the pre-selection cuts, and then the number of probe EM clusters that have HMx7 < 12 in CC and HMx8 < 10 in EC region is taken as the numerator. The efficiencies for CC phi-mod boundary electrons and phi-mod center electrons are measured separately.

The efficiency of electron ID is measured as a 2-dimensional function of cluster E_T and detector η. The measured efficiencies are shown in Fig. 6.3 for data and Fig. 6.4 for MC. The scale factors of data versus MC are shown in Fig. 6.5.
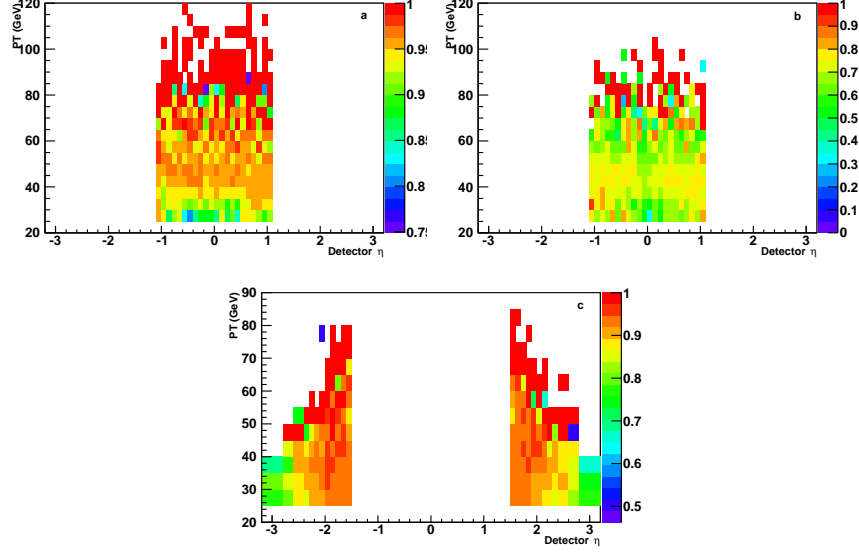
Figure 6.3: Electron ID efficiency as a function of E_T and detector η for RunIIb data. (a) CC phi-mod center electrons; (b) CC phi-mod boundary electrons; (c) EC electrons.
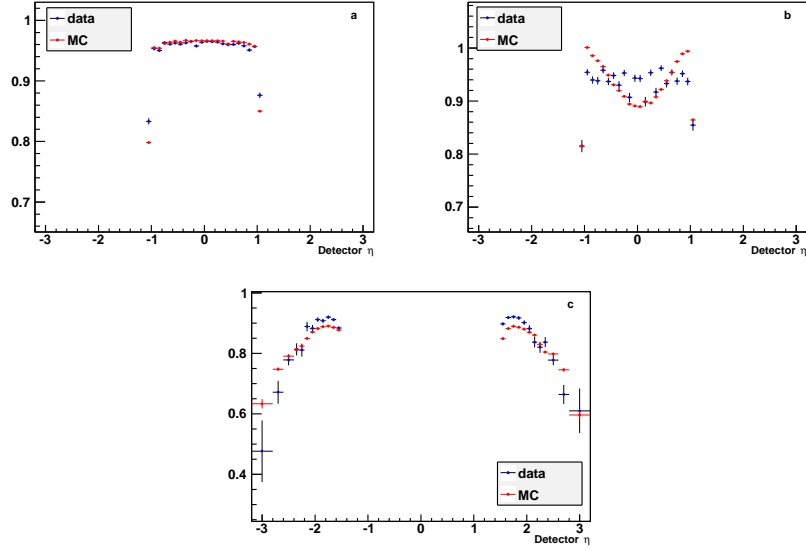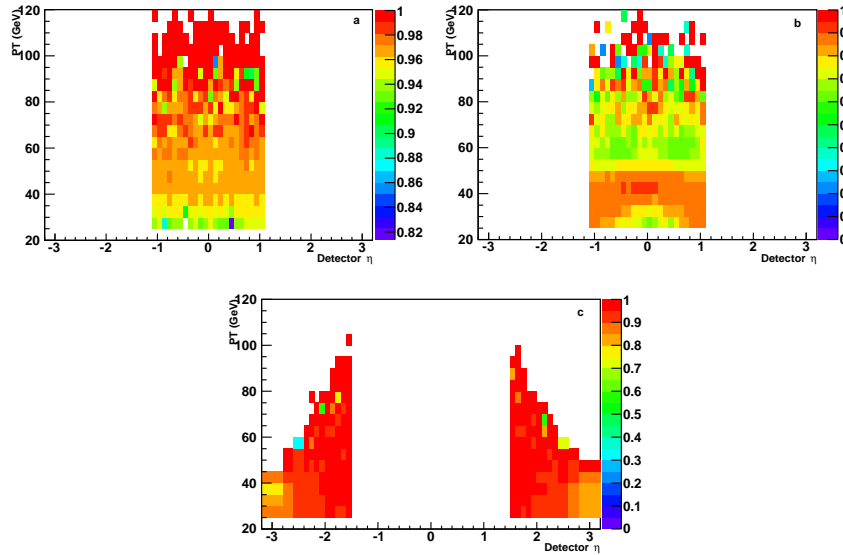

Figure 6.4: Electron ID efficiency as a function of E_T and detector η for RunIIb MC. (a) CC phi-mod center electrons; (b) CC phi-mod boundary electrons; (c) EC electrons.
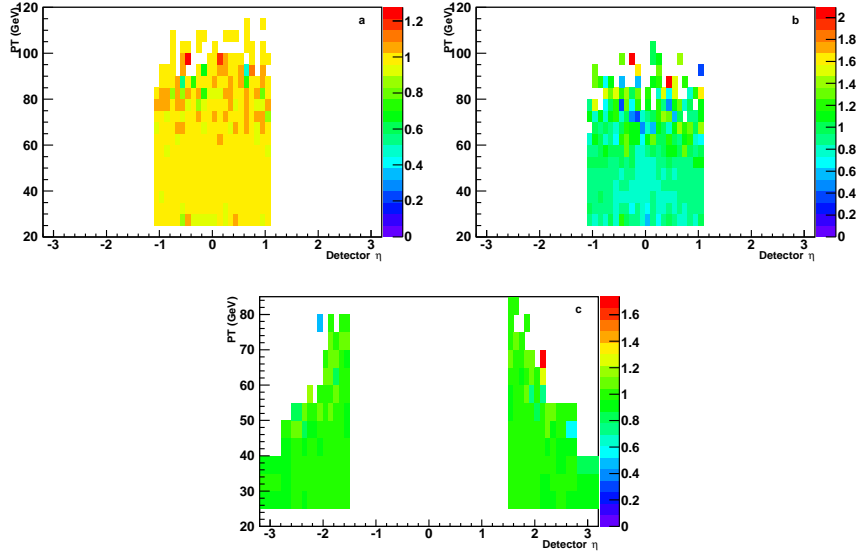
Figure 6.5: The data/MC ratios of electron ID efficiency as a function of E_T and detector η for RunIIb. (*a*) CC phi-mod center electrons; (*b*) CC phi-mod boundary electrons; (*c*) EC electrons.

6.3.4 Electron track match efficiency

Having analyzed calorimeter-based electron ID efficiency, we investigate spatial track match efficiency for electrons. The probe EM cluster is selected with the following requirements:

- $E_T > 25$ GeV;

- ID = 10 or ± 11, iso < 0.15(CC) or 0.1(EC), emf > 0.9, HMx7 < 12(CC) or Hmx8 < 10(EC);

- $\Delta\phi$ (tag electron, probe electron) > 2.

For the EM cluster track matching efficiency measurement, the number of EM clusters passing the above probe criteria is taken as the denominator. Then, the number of probe EM clusters that have a spacial matched track passing all track match selections is taken as the numerator. The track match efficiency is measured as a function of electron E_T and physics η. Note that since tracks of different types in the EC region are almost geometrically independent in different η bins, the EC electron track efficiency measured against η is not categorized into different types.

The track match efficiencies are shown in Fig. 6.6 for data and Fig. 6.7 for MC. The data/MC scale factors are shown in Fig. 6.8.

6.3.5 Uncertainties

To compensate for the detector response difference between the simulation and the data, the data to MC ratios of preselection, ID and track match efficiencies, depicted in Fig. 6.2, 6.5 and 6.8, are applied successively to simulated electrons with corresponding detector η or (p_T, η)
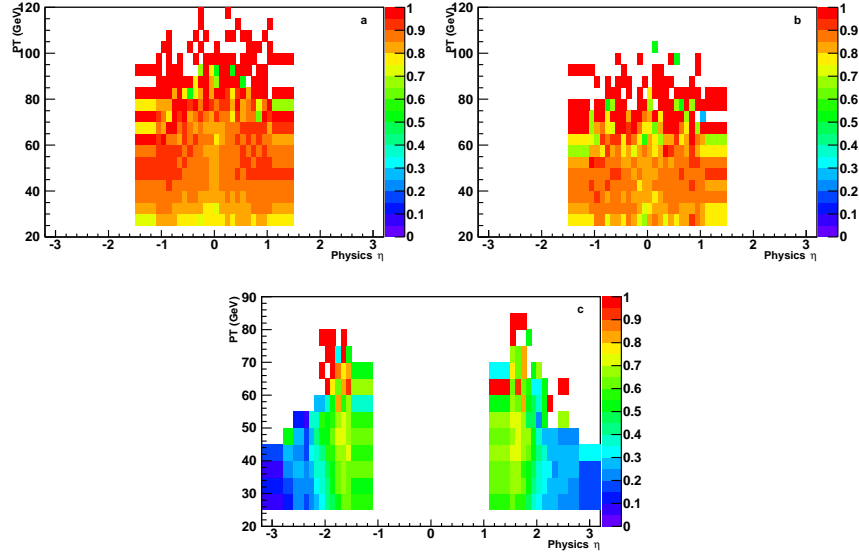
Figure 6.6: Track match efficiency as a function of E_T and physics η for RunIIb data. (a) CC phi-mod center electrons; (b) CC phi-mod boundary electrons; (c) EC electrons.
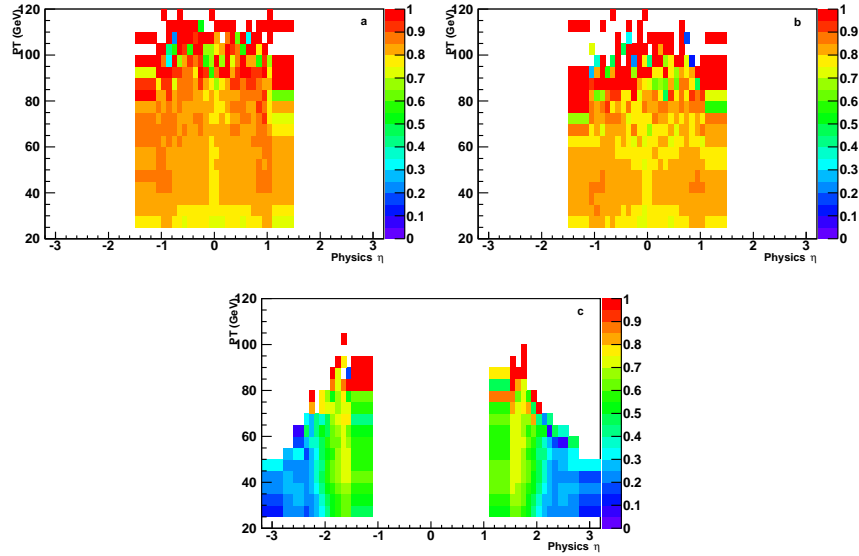
Figure 6.7: Track match efficiency as a function of E_T and physics η for RunIIb MC. (a) CC phi-mod center electrons; (b) CC phi-mod boundary electrons; (c) EC electrons.

bins. The statistical fluctuations of the ratios are used to estimate the systematic uncertainty arising from selection efficiency corrections.

6.3.6 Forward and backward efficiency

The weak-mixing angle measurement is neither sensitive to the absolute value of efficiencies nor to the scale factors between data and MC, since these factors would cancel out in the A_{FB}
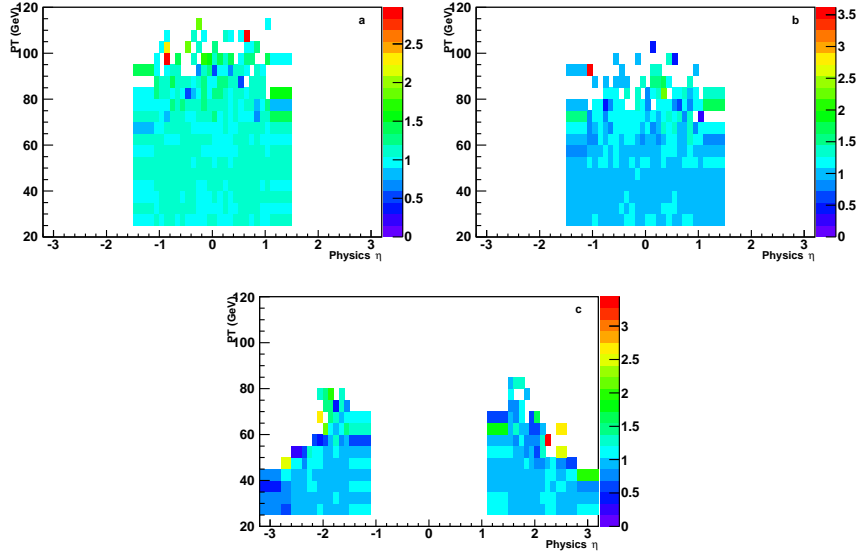
Figure 6.8: The data/MC ratios of track match efficiency as a function of E_T and physics η for RunIIb. (*a*) CC phi-mod center electrons; (*b*) CC phi-mod boundary electrons; (*c*) EC electrons.

distribution (but only if the selections do not distinguish between forward and backward events). Fig. 6.9 shows the p_T and η_{det} distributions in data. No apparent difference can be found. The efficiencies measured using forward and backward events are shown in Fig. 6.10.

Therefore, the efficiency corrections measured from all events are consistent in forward and backward events.

6.4 MC Reweightings

6.4.1 Instantaneous luminosity and vertex z reweighting

Data and MC have different instantaneous luminosity and primary vertex distributions. Additional reweightings for these variables are applied to the MC.

The instantaneous luminosity for data and MC, and the reweighting scale of data versus MC applied to the simulations, are depicted in Fig. 6.11.

The vertex z reweighting is done by applying a smearing factor. The distributions before and after reweighting are shown in Fig. 6.12 and Fig. 6.13

6.4.2 $M_{Z/\gamma*}$ reweighting

A mass-dependent K-factor is introduced to include higher order QCD corrections on the Z/γ^* boson invariant mass distribution. The K-factor is defined as [27]:

$$K = \frac{\sigma_{NNLO}\text{with NLO PDF}}{\sigma_{LO}\text{with LO PDF}} \tag{6.4}$$

The next-to-next-to-leading-order (NNLO) cross sections are obtained from the calculation of Hamberg *et. al.* [28]. The K-factor as a function of M_{ee} is given in Tab. 6.1 [29], where it varies
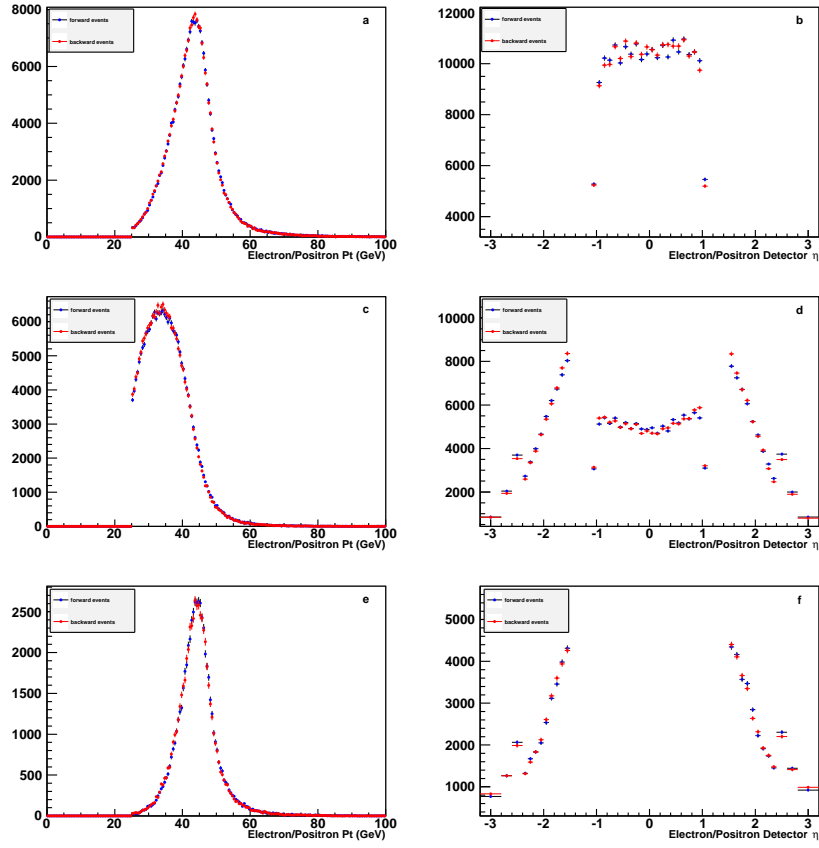
Figure 6.9: Kinematic distributions in RunIIb Forward/Backward data. (*a*) CC-CC p_T; (*b*) CC-CC detector η; (*c*) CC-EC p_T; (*d*) CC-EC detector η; (*e*) EC-EC p_T; (*f*) EC-EC detector η;

from 1.30 at $M = 50$ GeV to 1.38 at $M = 600$ GeV, increasing by $\sim 6\%$.

M_{DY} (GeV)	NNLO K factor
50.00	1.30
75.00	1.34
91.12	1.36
100.00	1.37
150.00	1.40
200.00	1.41
250.00	1.41
300.00	1.41
400.00	1.40
500.00	1.39
600.00	1.38

Table 6.1: The NNLO K factor as a function of invariant mass.
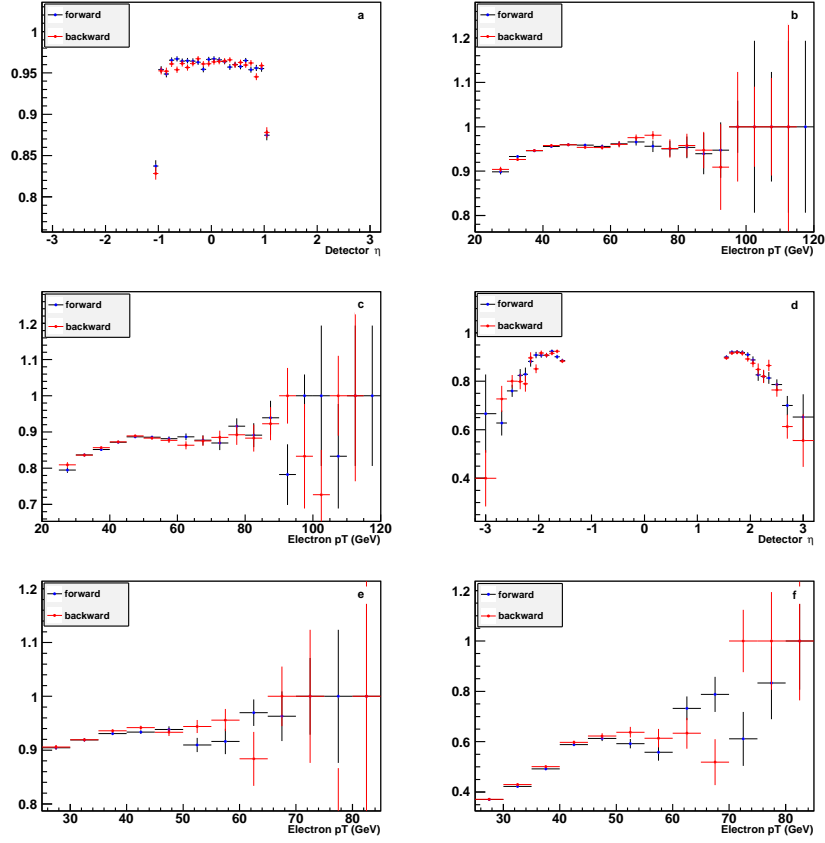
Figure 6.10: Forward and backward efficiencies in RunIIb data. (*a*) CC pre-selection efficiency vs. detector η; (*b*) CC EMID efficiency vs. p_T; (*c*) CC track-match efficiency vs. p_T; (*d*) EC pre-selection efficiency vs. detector η; (*e*) EC EMID efficiency vs. p_T; (*f*) EC track-match efficiency vs. p_T.
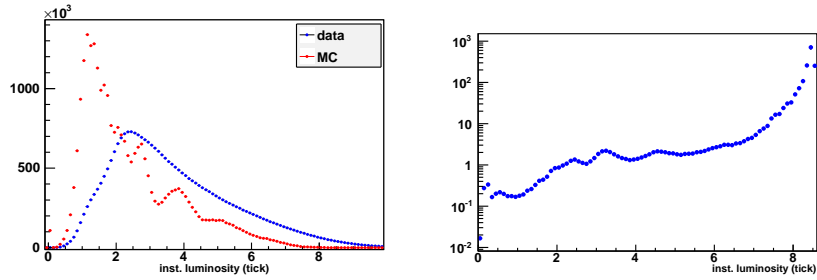
Figure 6.11: The instantaneous luminosity in RunIIb data and MC (Left) and the scale factor (Right).

6.4.3 Zp_T and y_Z reweighting

The ResBos generator [30] has been proven to give a more accurate theoretical description of the Z/γ^* boson transverse momentum and rapidity distributions compared to PYTHIA. A two-dimensional boson p_T and y re-weighting scheme developed by S. Yacoob *et. al.* [31] was applied to PYTHIA-based simulations. The reweighting factors as a 2D function of boson p_T and

58
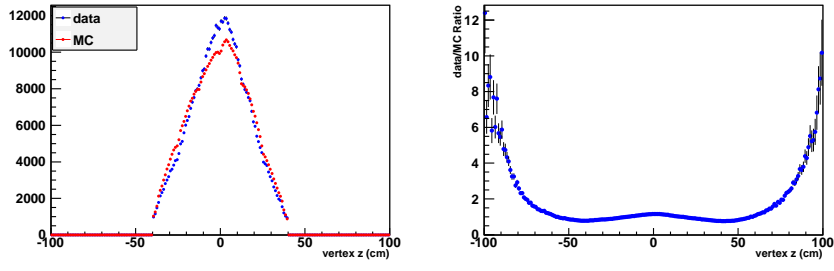
Figure 6.12: The vertex z in RunIIb data and MC (without smearing).
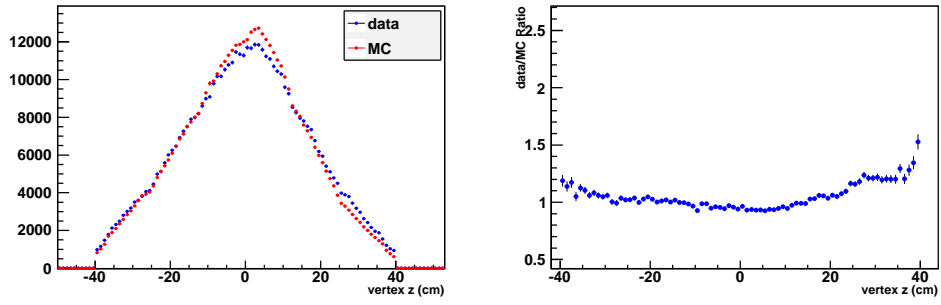
Figure 6.13: The vertex z in RunIIb data and MC (with smearing).

rapidity are shown in Fig. 6.14.
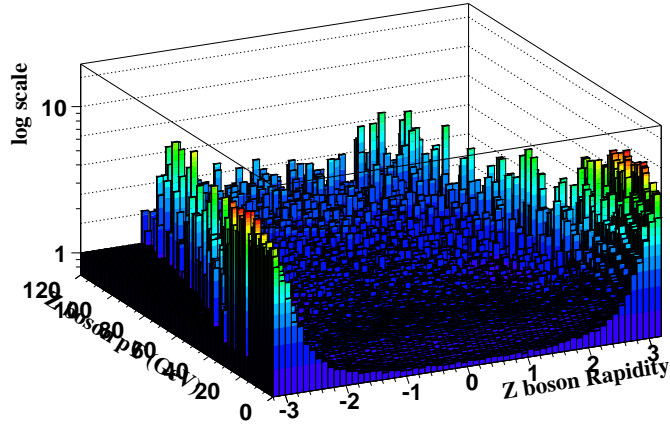
Figure 6.14: The boson p_T and rapidity reweighting factor.

6.5 Charge mis-identification

6.5.1 Effect of charge mis-identification

Charge measurement is important to this analysis, since we rely on the track charge to determine whether the selected EM cluster is an electron or a positron and classify the event as forward or backward accordingly.

For CC-CC events, we require that the two EM clusters must be matched to oppositely charged tracks. For CC-EC events, we require a track match for only the CC electron. Thus, the mis-identification probability in CC-EC events is higher. For EC-EC events, the mis-identification probability is even higher due to a lack of CFT coverage in the EC region.

The measured A_{FB} distribution is different from the true one due to the charge mis-identification. For a specific mass bin, the A_{FB} value can be expressed as

$$A_{FB}^{true} = \frac{N_{true}^F - N_{true}^B}{N_{true}^F + N_{true}^B}, \qquad A_{FB}^{meas} = \frac{N_{meas}^F - N_{meas}^B}{N_{meas}^F + N_{meas}^B} \tag{6.5}$$

where N_{true}^F, N_{true}^B, N_{meas}^F and N_{meas}^B are the numbers of the true forward/backward events and the measured ones in the mass bin, respectively.

For CC-CC events, we have:

$$
\begin{aligned}
A_{FB}^{meas} &= \frac{N_{meas}^F - N_{meas}^B}{N_{meas}^F + N_{meas}^B} \\
&= \frac{[(1-f_{cc})^2 N_{true}^F + f_{cc}^2 N_{true}^B] - [(1-f_{cc})^2 N_{true}^B + f_{cc}^2 N_{true}^F]}{[(1-f_{cc})^2 N_{true}^F + f_{cc}^2 N_{true}^B] + [(1-f_{cc})^2 N_{true}^B + f_{cc}^2 N_{true}^F]} \\
&= \frac{(1-2f_{cc})}{(1-2f_{cc}+2f_{cc}^2)} A_{FB}^{true}
\end{aligned}
$$

where f_{cc} denotes the CC electron charge mis-identification rate.

For CC-EC events, we have:

$$
\begin{aligned}
A_{FB}^{meas} &= \frac{N_{meas}^F - N_{meas}^B}{N_{meas}^F + N_{meas}^B} \\
&= \frac{[N_{true}^F + f_{cc}N_{true}^B - f_{cc}N_{true}^F] - [N_{true}^B - f_{cc}N_{true}^B + f_{cc}N_{true}^F]}{[N_{true}^F + f_{cc}N_{true}^B - f_{cc}N_{true}^F] + [N_{true}^B - f_{cc}N_{true}^B + f_{cc}N_{true}^F]} \\
&= (1-2f_{cc})A_{FB}^{true}
\end{aligned}
$$

For EC-EC events, we have:

$$
\begin{aligned}
A_{FB}^{meas} &= \frac{N_{meas}^F - N_{meas}^B}{N_{meas}^F + N_{meas}^B} \\
&= \frac{[N_{true}^F + f_{ec}N_{true}^B - f_{ec}N_{true}^F] - [N_{true}^B - f_{ec}N_{true}^B + f_{ec}N_{true}^F]}{[N_{true}^F + f_{ec}N_{true}^B - f_{ec}N_{true}^F] + [N_{true}^B - f_{ec}N_{true}^B + f_{ec}N_{true}^F]} \\
&= (1-2f_{ec})A_{FB}^{true}
\end{aligned}
$$

where f_{ec} denotes the EC electron charge mis-identification rate.

The measured A_{FB} values are smaller than the true values and the difference is determined by the charge mis-identification rate. If the mis-identification rate $f_{cc(ec)}$ is about 50%, which means that a track has an equal probability to be identified as positive and negative, then there is no way to get non-zero A_{FB}, for $1 - 2f_{cc(ec)} = 1 - 2 \times 50\% = 0$.

EC track type	data(%)	MC(%)
type2	0.960 ± 0.077	0.478 ± 0.013
type3	3.626 ± 0.075	1.723 ± 0.013
type4	9.044 ± 0.135	4.976 ± 0.024

Table 6.2: Charge misID rate for EC electrons.

6.5.2 Determination of Charge mis-identification

The charge mis-identification rate for CC electrons is only measured in CC-CC events with $75 < M_{ee} < 105$ GeV, using the same selection cuts as those employed for the signal CC-CC events except for the opposite charge requirement. The charge misID rate is then given by

$$f_{cc} = \frac{1}{2} \frac{N_{SS}}{N_{OS} + N_{SS}} \tag{6.6}$$

where $N_{SS}(N_{OS})$ is the total number of same-sign(opposite-sign) events in the Z mass peak region. The same method is applied to data and MC events. The average charge misID rate for CC electrons is found to be $\langle f_{cc} \rangle = (0.236 \pm 0.007)\%$ for data and $\langle f_{cc} \rangle = (0.080 \pm 0.001)\%$ for MC events. The charge misID is roughly a factor of 3 larger in data than in MC. The main reasons for the data-MC difference are an insufficient amount of tracking system material in simulation, and the imperfect alignment of the detector.

The charge mis-identification rate for EC electrons is measured in CC-EC events with $75 < M_{ee} < 105$ GeV. EC electrons are also required to have matched tracks. The charge misID rate for EC electrons is given by

$$f_{ec} = \frac{\frac{N_{SS}}{N_{SS} + N_{OS}} - f_{cc}}{1 - 2 f_{cc}} \tag{6.7}$$

The EC charge misID rates are measured separately for different EC track types, as shown in Tab. 6.2.

The charge mis-ID rate in MC is scaled to match the rate in data. We randomly change the track charge of an electron to the opposite sign by a probability of R:

$$R = \frac{f_{data} - f_{mc}}{1 - 2 f_{mc}}. \tag{6.8}$$

The values of R for MC electrons are shown in Tab. 6.3, and the statistical uncertainties are taken as the systematic error of charge mis-identification.

	R value
CC type1	0.00156 ± 0.00007
EC type2	0.00487 ± 0.077
EC type3	0.01971 ± 0.075
EC type4	0.04518 ± 0.135

Table 6.3: R values for MC electrons mis-identification smearing.

Chapter 7

Backgrounds

Sources of background to the Drell-Yan $p\bar{p} \to Z/\gamma^* + X \to ee + X$ process are:

- QCD multi-jet events, where jets are misidentified as electrons;

- $Z/\gamma^* \to \tau^+\tau^- \to e^+e^-\nu_\tau\nu_e\bar{\nu}_\tau\bar{\nu}_e$;

- $W + X \to e\nu + X$, where X is a jet or photon misidentified as an electron;

- $\gamma + \gamma$, where the two γs are misidentified as electrons;

- $W^+W^- \to e^+e^-\nu_e\bar{\nu}_e$;

- $W^\pm Z$, where $W \to e\nu$ and $Z \to e^+e^-$.

- $t\bar{t} \to Wb + W\bar{b} \to e\nu b + e\nu\bar{b}$.

The determination of A_{FB} requires knowledge of the number of background events and the forward-backward charge asymmetry of those events in each mass bin.

The QCD multi-jet is the dominant background and is measured from data. The background of $W + X$ is estimated by using ALPGEN + PYTHIA MC. Other backgrounds are determined by using corrected PYTHIA MC. The QCD background level is less than 1% in CC-CC and 3% in CC-EC and EC-EC events. The contamination from $W + X$ and other backgrounds is negligible. In general, the contribution from backgrounds are very small to the A_{FB} distribution around Z pole.

7.1 $W + X$ background

$W + X$ background is estimated with ALPGEN + PYTHIA MC. We include two uncertainties to cover the mismodeling effects:

- Statistical uncertainty of selected $W + X$ events.

- RunIIb integrated luminosity uncertainty of 4.2%.

Mass Range (GeV)	CC-CC		CC-EC		EC-EC	
	Forward	Backward	Forward	Backward	Forward	Backward
$60 < M_{ee} < 70$	5.71±1.50	4.06±1.04	48.29±5.92	18.13±3.45	23.25±5.78	10.53±2.54
$70 < M_{ee} < 75$	5.86±2.24	2.96±1.08	26.86±3.89	10.64±2.82	5.96±1.95	3.81±1.11
$75 < M_{ee} < 81$	2.58±1.12	3.18±1.20	66.07±9.79	18.32±3.24	8.00±2.33	5.54±1.79
$81 < M_{ee} < 86.5$	3.71±1.00	2.43±0.79	52.94±5.54	17.28±3.27	7.58±2.44	4.59±1.53
$86.5 < M_{ee} < 89.5$	0.95±0.61	1.28±0.82	23.07±3.75	14.10±8.21	2.23±0.96	1.60±1.01
$89.5 < M_{ee} < 92$	1.47±0.66	1.53±0.74	17.24±2.80	7.24±1.84	0.99±0.46	1.79±1.10
$92 < M_{ee} < 97$	4.16±1.24	1.82±0.72	39.11±4.45	13.25±2.60	2.39±0.98	3.62±1.44
$97 < M_{ee} < 105$	5.33±1.36	2.13±0.70	40.71±4.40	13.85±2.50	3.02±1.58	3.42±1.35
$105 < M_{ee} < 115$	6.55±1.91	1.70±0.61	57.51±5.61	20.63±4.27	2.91±1.41	1.04±0.42
$115 < M_{ee} < 130$	5.28±1.74	2.55±1.05	89.31±8.59	30.98±4.08	1.32±0.62	0.85±0.37

Table 7.1: Number of forward and backward events in $W + X$ background expected in RunIIb.

Expected event yields for each process are shown in Tab. 7.1. The contribution of $W + X$ background estimated from MC is less than 0.3%.

[H]

7.2   Other EW backgrounds

EW backgrounds other than $W + X$ are estimated by using the PYTHIA MC, with NLO QCD corrections applied.

The NLO cross sections are $\sigma(Z/\gamma^* \to \tau\tau) = 252 \pm 9$ pb [32], $\sigma(WW \to e\nu e\nu) = 12.1 \pm 0.8$ pb and $\sigma(WZ \to 3l + \nu) = 0.1145 \pm 0.0458$ pb [33, 34].

The simulated events for each process which pass the selection requirements are used to determine both the invariant mass distributions and the expected numbers of forward and backward events, as shown in Tab. 7.2 to Tab. 7.6.

Mass Range (GeV)	CC-CC		CC-EC		EC-EC	
	Forward	Backward	Forward	Backward	Forward	Backward
$60 < M_{ee} < 70$	5.72±0.40	8.18±0.49	1.48±0.20	3.45±0.36	0.49±0.10	0.63±0.12
$70 < M_{ee} < 75$	3.68±0.32	3.92±0.34	0.79±0.13	1.78±0.24	0.21±0.07	0.33±0.10
$75 < M_{ee} < 81$	4.43±0.36	4.71±0.37	1.36±0.19	1.87±0.21	0.44±0.10	0.21±0.07
$81 < M_{ee} < 86.5$	4.08±0.38	4.71±0.47	1.32±0.19	2.25±0.25	0.22±0.06	0.21±0.07
$86.5 < M_{ee} < 89.5$	2.01±0.24	1.93±0.23	1.11±0.18	1.17±0.17	0.01±0.01	0.04±0.03
$89.5 < M_{ee} < 92$	1.73±0.21	1.81±0.24	0.55±0.12	0.87±0.14	0.07±0.03	0.00±0.00
$92 < M_{ee} < 97$	2.72±0.29	3.08±0.30	1.61±0.22	1.69±0.23	0.16±0.08	0.10±0.05
$97 < M_{ee} < 105$	4.36±0.39	4.29±0.39	2.44±0.25	3.42±0.35	0.14±0.07	0.16±0.06
$105 < M_{ee} < 115$	4.75±0.37	5.42±1.14	3.22±0.28	4.51±0.63	0.19±0.06	0.12±0.05
$115 < M_{ee} < 130$	6.18±0.47	5.00±0.40	4.58±0.40	4.95±0.37	0.10±0.05	0.13±0.05

Table 7.2: Number of forward and backward events in WW background expected in RunIIb.

Mass Range (GeV)	CC-CC		CC-EC		EC-EC	
	Forward	Backward	Forward	Backward	Forward	Backward
$60 < M_{ee} < 70$	0.32±0.01	0.37±0.018	0.17±0.01	0.23±0.02	0.04±0.00	0.05±0.00
$70 < M_{ee} < 75$	0.27±0.01	0.32±0.017	0.16±0.01	0.23±0.02	0.04±0.00	0.03±0.00
$75 < M_{ee} < 81$	0.65±0.02	0.64±0.024	0.34±0.01	0.31±0.01	0.08±0.01	0.06±0.00
$81 < M_{ee} < 86.5$	1.92±0.04	1.77±0.040	0.99±0.03	0.83±0.02	0.23±0.02	0.18±0.01
$86.5 < M_{ee} < 89.5$	3.36±0.07	2.97±0.055	1.73±0.04	1.38±0.03	0.39±0.01	0.37±0.02
$89.5 < M_{ee} < 92$	4.04±0.06	3.83±0.074	2.30±0.04	1.99±0.04	0.55±0.02	0.54±0.02
$92 < M_{ee} < 97$	5.30±0.10	4.94±0.070	3.10±0.05	2.52±0.04	0.66±0.02	0.62±0.02
$97 < M_{ee} < 105$	1.37±0.03	1.31±0.036	0.89±0.02	0.85±0.03	0.12±0.01	0.11±0.00
$105 < M_{ee} < 115$	0.42±0.02	0.44±0.022	0.51±0.02	0.52±0.02	0.02±0.01	0.02±0.00
$115 < M_{ee} < 130$	0.34±0.01	0.37±0.018	0.81±0.13	0.69±0.02	0.01±0.01	0.01±0.00

Table 7.3: Number of forward and backward events in WZ background expected in RunIIb.

Mass Range (GeV)	CC-CC		CC-EC		EC-EC	
	Forward	Backward	Forward	Backward	Forward	Backward
$60 < M_{ee} < 70$	4.81±0.46	4.82±0.48	0.63±0.15	0.53±0.15	0.05±0.03	0.07±0.05
$70 < M_{ee} < 75$	2.70±0.33	2.67±0.36	0.27±0.08	0.47±0.12	0.08±0.04	0.00±0.00
$75 < M_{ee} < 81$	3.96±0.43	2.52±0.30	0.39±0.10	0.80±0.16	0.04±0.04	0.06±0.05
$81 < M_{ee} < 86.5$	2.66±0.32	2.49±0.30	0.37±0.11	0.50±0.13	0.00±0.00	0.06±0.04
$86.5 < M_{ee} < 89.5$	1.67±0.30	1.55±0.22	0.25±0.09	0.19±0.06	0.00±0.00	0.06±0.04
$89.5 < M_{ee} < 92$	1.11±0.20	1.25±0.24	0.26±0.08	0.27±0.10	0.01±0.01	0.00±0.00
$92 < M_{ee} < 97$	2.88±0.38	2.13±0.30	0.63±0.14	0.75±0.16	0.13±0.08	0.00±0.00
$97 < M_{ee} < 105$	3.41±0.35	4.62±0.49	0.75±0.16	0.95±0.23	0.00±0.00	0.03±0.03
$105 < M_{ee} < 115$	3.34±0.36	4.12±0.41	1.16±0.20	0.68±0.13	0.00±0.00	0.00±0.00
$115 < M_{ee} < 130$	5.09±0.45	5.52±0.47	1.64±0.25	1.71±0.24	0.00±0.00	0.00±0.00

Table 7.4: Number of forward and backward events in $t\bar{t}$ background expected in RunIIb.

Mass Range (GeV)	CC-CC		CC-EC		EC-EC	
	Forward	Backward	Forward	Backward	Forward	Backward
$60 < M_{ee} < 70$	65.75±4.89	69.37±6.29	34.03±3.62	24.34±2.77	26.67±2.82	27.37±3.24
$70 < M_{ee} < 75$	22.44±2.72	23.36±2.86	24.92±2.96	11.78±1.98	9.04±1.66	10.28±2.66
$75 < M_{ee} < 81$	21.32±3.24	13.44±1.98	13.40±2.08	13.39±2.23	5.77±1.17	4.02±1.11
$81 < M_{ee} < 86.5$	6.97±1.40	3.30±0.83	6.12±1.16	4.57±1.35	0.80±0.37	1.37±0.63
$86.5 < M_{ee} < 89.5$	2.07±0.79	0.52±0.09	1.95±0.58	0.64±0.26	0.53±0.32	0.19±0.17
$89.5 < M_{ee} < 92$	0.55±0.05	0.31±0.04	2.14±0.73	0.41±0.26	0.06±0.02	0.12±0.10
$92 < M_{ee} < 97$	1.59±0.33	1.04±0.46	2.20±0.56	0.58±0.33	0.12±0.05	0.22±0.19
$97 < M_{ee} < 105$	1.86±0.14	0.86±0.22	3.74±0.98	0.35±0.08	0.65±0.56	0.04±0.01
$105 < M_{ee} < 115$	2.26±0.21	0.79±0.07	2.25±0.30	1.47±0.58	0.05±0.01	0.03±0.01
$115 < M_{ee} < 130$	1.87±0.10	0.78±0.06	2.28±0.33	0.75±0.27	0.04±0.01	0.05±0.01

Table 7.5: Number of forward and backward events in $Z\tau\tau$ background expected in RunIIb.

Mass Range (GeV)	CC-CC		CC-EC		EC-EC	
	Forward	Backward	Forward	Backward	Forward	Backward
$60 < M_{ee} < 70$	0.17±0.129	0.02±0.01	4.91±1.36	6.03±1.44	25.77±3.64	24.73±2.93
$70 < M_{ee} < 75$	0.04±0.005	0.02±0.01	3.25±0.95	2.64±0.90	8.92±1.79	9.11±2.10
$75 < M_{ee} < 81$	0.44±0.364	0.67±0.64	6.73±1.63	3.54±1.15	8.21±1.76	7.28±1.74
$81 < M_{ee} < 86.5$	0.08±0.007	0.03±0.01	7.60±2.08	4.24±1.26	5.58±1.36	5.67±1.46
$86.5 < M_{ee} < 89.5$	0.06±0.006	0.01±0.01	3.76±1.24	5.22±1.31	3.85±1.32	1.98±0.71
$89.5 < M_{ee} < 92$	0.04±0.005	0.02±0.01	4.01±1.49	1.58±0.81	1.40±0.59	2.29±1.01
$92 < M_{ee} < 97$	0.11±0.009	0.05±0.01	5.19±1.36	3.84±1.24	3.03±1.14	2.04±0.81
$97 < M_{ee} < 105$	0.19±0.010	0.09±0.01	10.6±2.07	6.73±1.58	3.45±1.70	2.50±1.00
$105 < M_{ee} < 115$	0.29±0.013	0.13±0.01	6.03±1.41	4.67±1.26	3.08±1.36	2.98±1.35
$115 < M_{ee} < 130$	0.49±0.025	0.19±0.01	9.06±1.84	11.30±2.66	1.33±0.68	3.07±1.03

Table 7.6: Number of forward and backward events in $\gamma\gamma$ background expected in RunIIb.

7.3 QCD background

QCD multi-jet events contribute to instrumental background, where jets are mis-reconstructed as electrons. The QCD contribution is 2% - 3% in CC-EC and EC-EC events, but less than 1% in CC-CC events due to tighter track match requirements in that region.

7.3.1 QCD background shape

The shape of the invariant mass distribution of QCD background is found by inverting the electron shower shape requirement. In the CC region we require Hmx7 > 40 or track isolation > 3.5 GeV; In EC region we require Hmx8 > 40 or track isolation > 3.5 GeV. Track match requirements are removed both for CC and EC electrons.

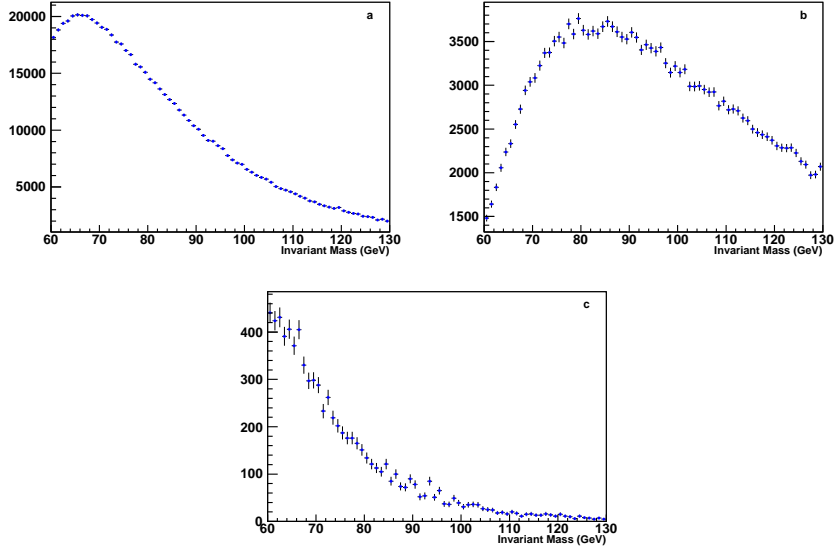The QCD shape around the Z mass peak region is shown in Fig. 7.1.

Figure 7.1: Shapes of QCD background around Z pole selected by reversed cuts, (a) CC-CC events, (b) CC-EC events and (c) EC-EC events.

7.3.2 Normalization

The normalization is measured by fitting the Z/γ^* invariant mass distributions of the signal MC and QCD background to the EW-background-subtracted data in the range $[60 - 130]$ GeV. The normalization factors are listed in Tab. 7.7. The fitting uncertainty is dominated by the differences between the QCD and signal templates, not from the fraction of QCD in data. As depicted in Fig. 7.1, most EC-EC QCD events are in the low-mass region, which is quite different from the shape of signal events around Z-pole, so the fitting uncertainty is smallest for EC-EC QCD events.

	QCD background in data
CC-CC	$0.517\% \pm 0.126\%$
CC-EC	$2.697\% \pm 0.114\%$
EC-EC	$3.723\% \pm 0.03\%$

Table 7.7: QCD background in data.

The number of QCD background events in each mass bin are shown in Tab. 7.8. We assume there is no asymmetry in di-jet background so the numbers of both forward and backward QCD events in a specific mass bin are set to half of the total number in that bin.

Mass	QCD in CC-CC	QCD in CC-EC	QCD in EC-EC
60.0 - 70.0	246.545 ± 60.086	532.084 ± 22.165	861.634 ± 7.638
70.0 - 75.0	138.348 ± 33.717	400.152 ± 16.956	333.894 ± 2.960
75.0 - 91.0	161.679 ± 39.403	546.701 ± 23.166	305.266 ± 2.706
81.0 - 86.5	139.921 ± 34.100	526.433 ± 22.307	204.829 ± 1.815
86.5 - 89.5	71.405 ± 17.402	290.212 ± 12.297	86.815 ± 0.770
89.5 - 92.0	56.452 ± 13.758	242.417 ± 10.272	65.211 ± 0.578
92.0 - 97.0	105.618 ± 25.740	478.104 ± 20.259	114.747 ± 1.017
97.0 - 105.0	145.258 ± 35.401	719.141 ± 30.472	122.097 ± 1.082
105.0 - 115.0	147.279 ± 35.893	831.04 ± 35.214	81.914 ± 0.726
115.0 - 130.0	164.757 ± 40.154	1062.050 ± 45.002	77.582 ± 0.688

Table 7.8: QCD background in each mass bin estimated in RunIIb.

7.4 Comparison between Data and Signal+backgrounds

Using the event selection and background estimation described above, we compare the Z boson invariant mass, $\cos\theta^*$ and electron/positron p_T of selected data and signal+QCD+EW backgrounds expectation.

The comparisons are shown from Fig. 7.2 to Fig. 7.4. Good agreement between data and SM prediction is observed for all distributions.
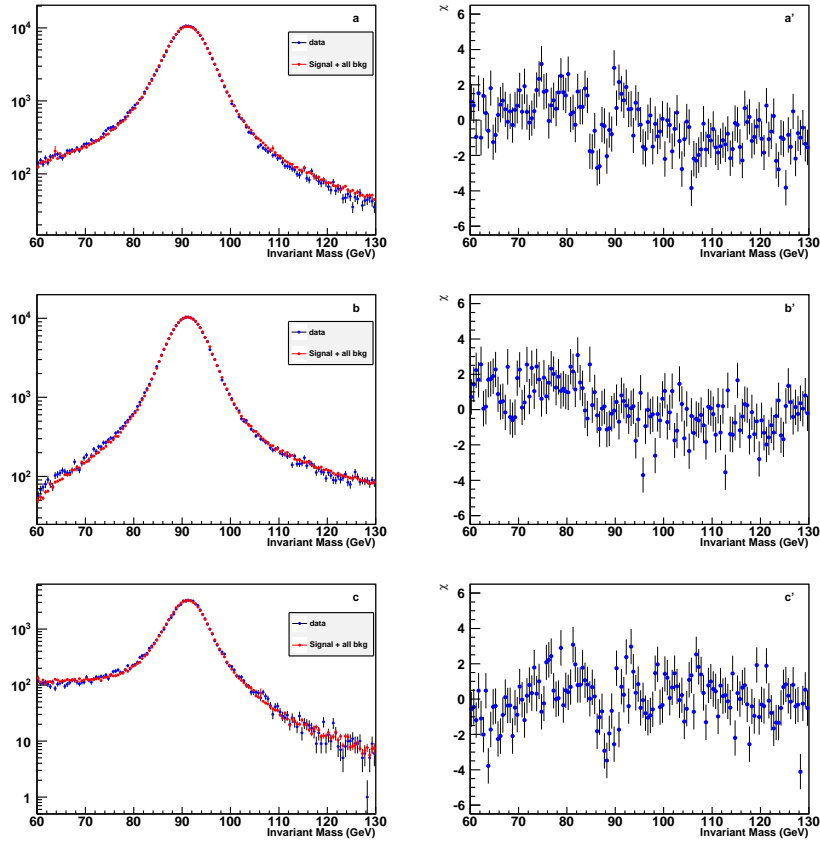
Figure 7.2: Invariant mass distributions of RunIIb. (a) CC-CC events, total $\chi^2 = 270$ (140 bins); (b) CC-EC events, total $\chi^2 = 240$ (140 bins); (c) EC-EC events, total $\chi^2 = 244$ (140 bins).

Figure 7.3: Electron/Positron p_T distributions of RunIIb. (a) CC-CC events, total $\chi^2 = 390$ (200 bins); (b) CC-EC events, total $\chi^2 = 190$ (200 bins); (c) EC-EC events, total $\chi^2 = 340$ (200 bins).

Figure 7.4: $cos\theta^*$ distribution of RunIIb. (a) CC-CC events, total $\chi^2 = 73$ (50 bins); (b) CC-EC events, total $\chi^2 = 117$ (50 bins); (c) EC-EC events, total $\chi^2 = 93$ (50 bins).
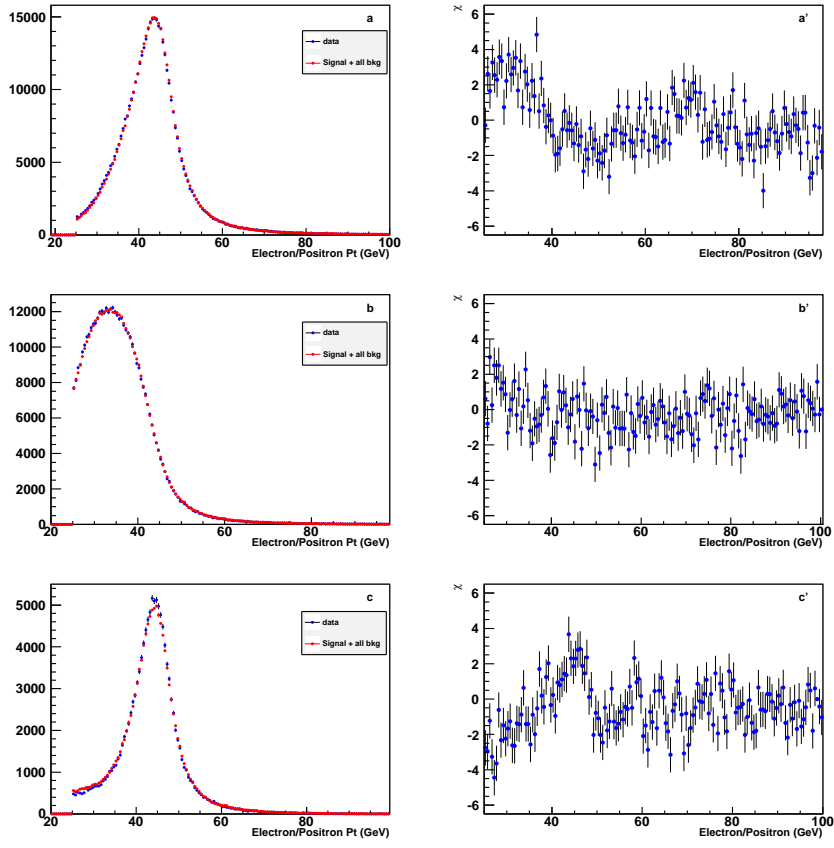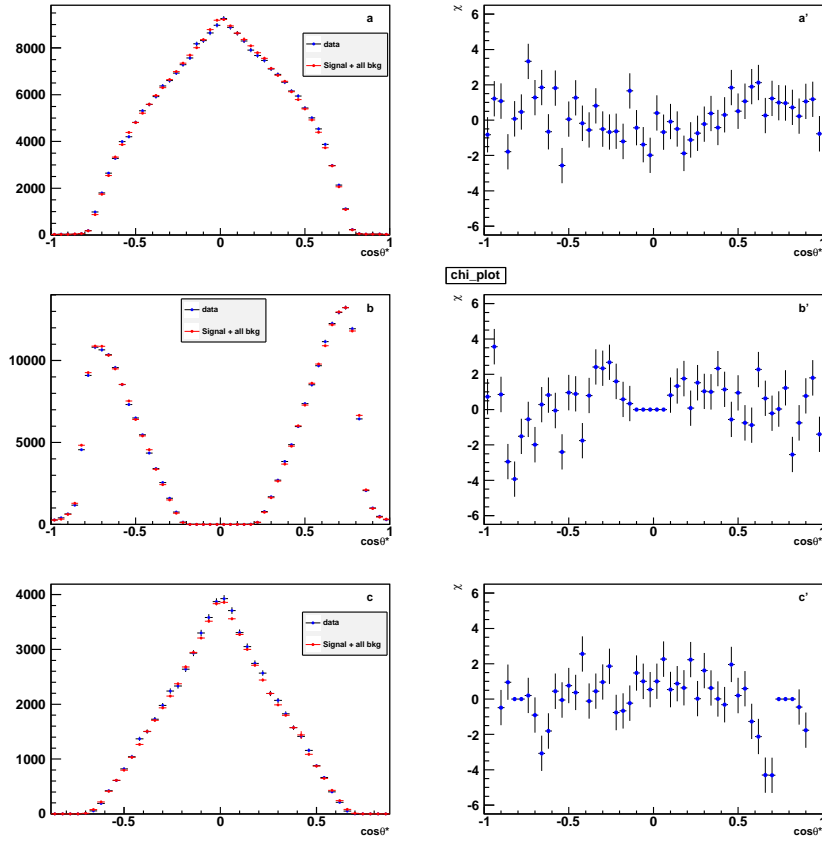
Chapter 8

Extraction of $\sin^2\theta_W$

8.1 Data-MC comparison for full RunII period

The previous chapters describe the strategy to achieve data-MC agreement using RunIIb samples as examples. From this chapter we will discuss the physical results of the weak mixing angle measurement and uncertainty estimation. All results from now on correspond to the full RunII data set (9.7 fb^{-1}). The M_{ee} distributions, collins angle $\cos\theta^*$ distributions and the A_{FB} distributions in the data compared to the signal MC + backgrounds are shown in Fig. 8.1 to Fig. 8.3.
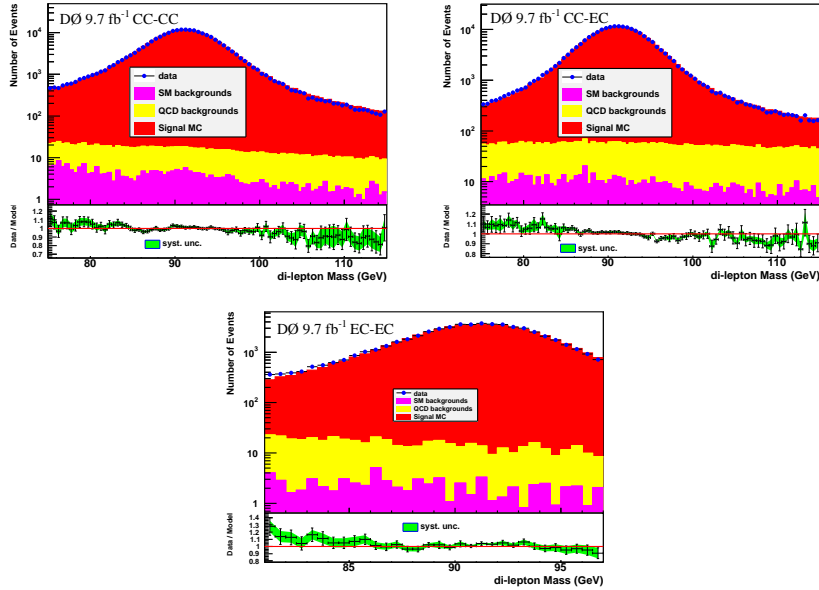

Figure 8.1: M_{ee} distributions in CC-CC, CC-EC and EC-EC events for the full data set comparison.
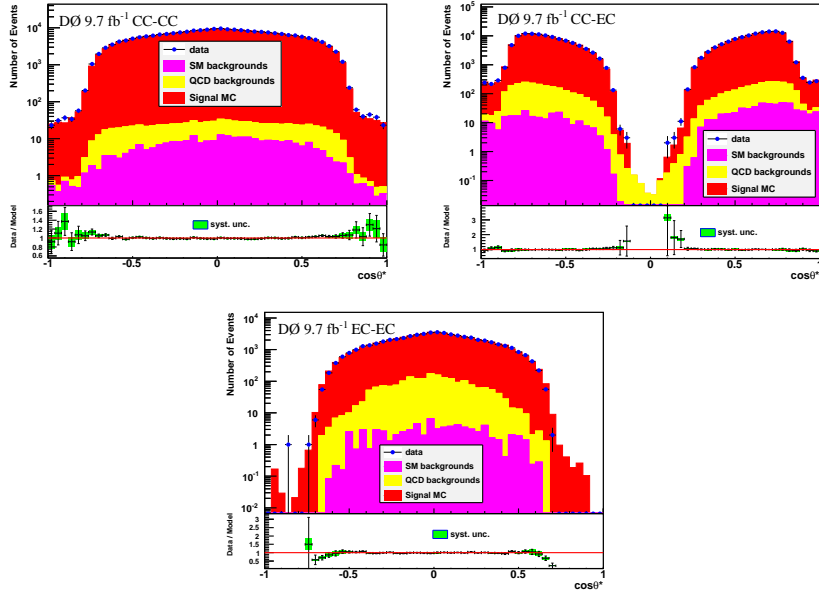
Figure 8.2: $\cos\theta^*$ distributions in CC-CC, CC-EC and EC-EC events for the full data set comparison.
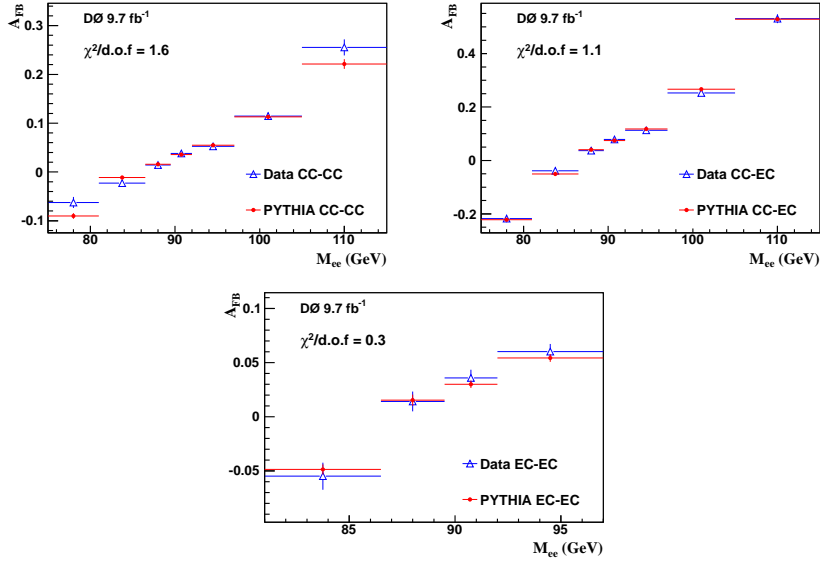
Figure 8.3: A_{FB} distributions in CC-CC, CC-EC and EC-EC events for the full data set comparison.

8.2 Reweighting MC samples to different input $\sin^2\theta_W$

The default full simulation MC samples were generated with fixed $\sin^2\theta_W = 0.232$. Samples at different values are needed to compare to data and extract the weak mixing angle. This is done by doing generator-level 2-dimensional $(M_{Z/\gamma^*} - \cos\theta^*)$ reweighting, which is the ratio of the 2D distributions between a specific $\sin^2\theta_W$ MC sample and the default one. The reweighting factor is obtained separately for CC-CC, CC-EC and EC-EC events. Electrons with physics

$|\eta| < 1.3$ at generator level are considered to be CC electrons while those with physics $|\eta| > 1.3$ are considered to be EC electrons. The 2D reweighting plots for $\sin\theta = 0.22552$ is shown in Fig. 8.4 as an example.
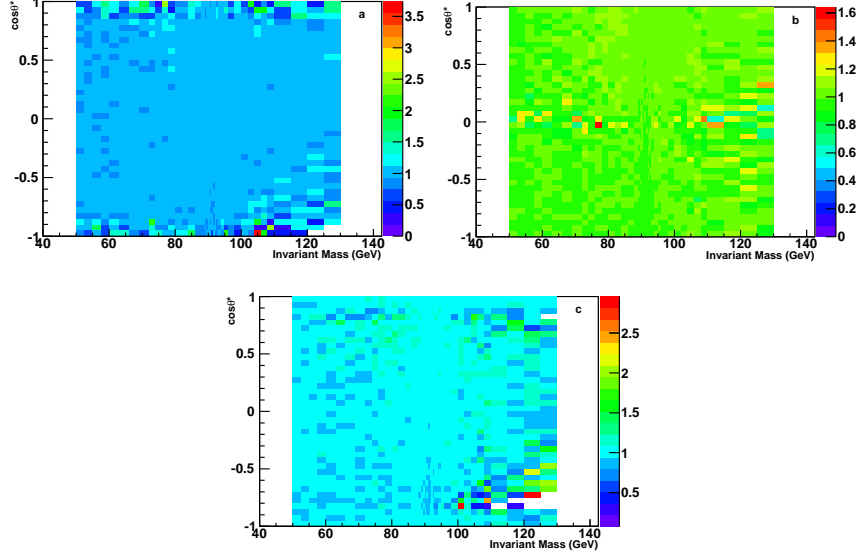
Figure 8.4: $M_{Z/\gamma^*} - \cos\theta^*$ 2d reweighting plots for $\sin\theta = 0.22552$. (a) CC-CC events; (b) CC-EC events; (c) EC-EC events.

In this case, 40 different full simulated templates for $\sin^2\theta_W$ are produced in the range from 0.22552 to 0.23722, with step size 0.0003. Fig. 8.5 shows the A_{FB} distributions acquired by reweighting the default MC ($\sin^2\theta_W = 0.232$) to $\sin^2\theta_W = 0.22552$ and $\sin^2\theta_W = 0.23722$.
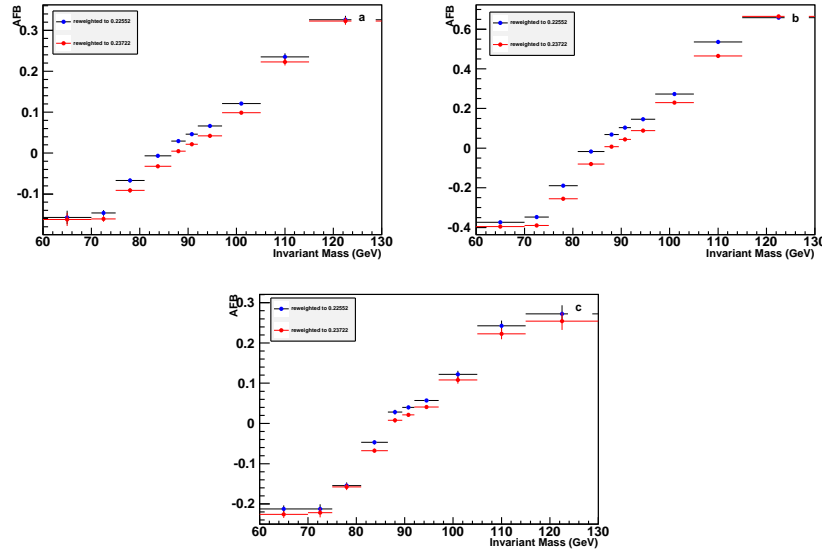
Figure 8.5: A_{FB} of the reweighted MC samples. (a) CC-CC events; (b) CC-EC events; (c) EC-EC events.

8.3 Extraction of $\sin^2 \theta_W$

The background subtracted raw A_{FB} distribution observed from data is compared to different $\sin^2 \theta_W$ MC models to extract the weak mixing angle. By using the raw A_{FB} instead of unfolded one, the uncertainties due to the unfolding method are eliminated.

The value of $\sin^2 \theta_W$ is measured by calculate a χ^2 from the comparison of the raw A_{FB} distribution in the data and each MC template The formula used for the χ^2 calculation is:

$$\chi^2 = \sum_{bin} \frac{(A_{FB}^{data} - A_{FB}^{MC})^2}{(\delta A_{FB}^{data})^2 + (\delta A_{FB}^{MC})^2}$$

The seven most sensitive bins around Z pole, namely in the mass range $75 < M_{ee} < 115$ GeV, are used to extract the weak mixing angle for CC-CC and CC-EC events. For EC-EC events, four bins in the mass range $81 < M_{ee} < 97$ GeV are used. Fig. 8.6 gives the χ^2 as a function of the $\sin^2 \theta_W$ inputs of the different reweighted full MC simulations.
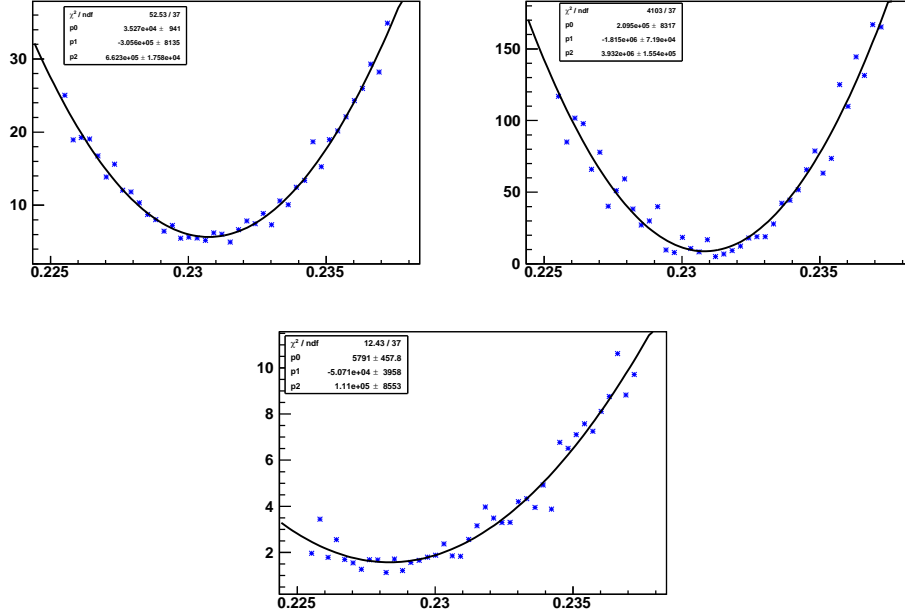
Figure 8.6: χ^2 between raw A_{FB} from data and different MC models, calculated using mass between 75 and 105 GeV. (*a*) CC-CC events; (*b*) CC-EC events; (*c*) EC-EC events.

We measure $\sin^2 \theta_W = 0.23142 \pm 0.00116$ using CC-CC events, $\sin^2 \theta_W = 0.23143 \pm 0.00047$ using CC-EC events and $\sin^2 \theta_W = 0.22977 \pm 0.00276$ using EC-EC events. Uncertainties are statistical only. The A_{FB} distribution is most sensitive to the $\sin^2 \theta_W$ in CC-EC events because the opening angle between the two electrons is larger. Therefore the uncertainty from CC-EC events is the smallest. The sensitivity for CC-CC and EC-EC events are similar. But there are much more CC-CC events than EC-EC, so the uncertainty from EC-EC events is larger than that from CC-CC events.

The combined results from CC-CC, CC-EC and EC-EC events are 0.23139 ± 0.00043(stat.). CC-EC is the dominate category in this measurement.

8.4 Higher order corrections

In order to have a consistent SM definition and make our result comparable with previous measurements, the PYTHIA interpretation of the weak mixing angle has been compared to the modified NLO RESBOS predictions, which uses different values of effective weak mixing angle for leptons and up or down quarks. RESBOS has more sophisticated treatment of electroweak effects. A 150M generator level MC sample generated by PYTHIA with $\sin^2 \theta_W = 0.23139$ and 40 templates generated by RESBOS with $\sin^2 \theta_W$ varying from 0.22552 to 0.23722 are used to estimate the high order correction. We compare the generator level A_{FB} distributions from PYTHIA and RESBOS using the same method described in Sec. 8.3. The best fitted value of $\sin^2 \theta_W$ in RESBOS is 0.00008 larger than the value in PYTHIA. The shift is added to the final result of $\sin^2 \theta_l^{\text{eff}}$. The leptonic effective weak mixing angle measured using DØ 9.7 fb^{-1} $Z/\gamma^* \to e^+ e^-$ data is then $\sin^2 \theta_l^{\text{eff}} = 0.23147 \pm 0.00043$.

Chapter 9

Systematic Uncertainties

Sources of systematic uncertainty includes electron energy calibration, energy resolution, efficiency measurement, background estimation, charge mi-identification measurement and the PDFs. The total contribution from systematic uncertainty is negligible compared to the statistical uncertainty. The systematic uncertainty itself, is also statistical dominated.

9.1 Energy Calibration

The energy calibration which shifts the energy scale, is the most sensitive one to A_{FB}. However, with a new method applied, the uncertainty from electron energy scale is significantly reduced. The systematic uncertainty on $\sin^2 \theta_W$ from energy scale is estimated by calculating the deviation of the M_{ee} peak after calibration from the LEP measured Z boson mass (δM), in all η_{det} regions. δM is then propagated into an overall scale factors α_{cc} and α_{ec}:

$$
\begin{aligned}
\delta M &= \sqrt{\frac{\sum_{i=0}^{N_\eta}(M_i - 91.1876)^2}{N_\eta(N_\eta - 1)}} \\
\frac{\delta M_{cc}}{91.1876} &= \frac{\delta \alpha_{cc}}{\alpha_{cc}} \\
\frac{\delta M_{ec}}{91.1876} &= \frac{1}{2}\sqrt{\left(\frac{\delta \alpha_{cc}}{\alpha_{cc}}\right)^2 + \left(\frac{\delta \alpha_{ec}}{\alpha_{ec}}\right)^2}.
\end{aligned}
$$

The difference between $\sin^2 \theta_W$ measured with original calibration, and the value measured with additional α_{cc} and α_{ec} applied to the MC templates is taken as the uncertainty from energy scale. The systematic uncertainty from energy smear is estimated by varying the smearing factor with $\pm 1\sigma$.

- 0.00003 due to energy calibration and energy scale for CC-CC events.

- 0.00001 due to energy smearing for CC-CC events.

- 0.00001 due to energy calibration and energy scale for CC-EC events.

- 0.00002 due to energy smearing for CC-EC events.

- 0.00004 due to energy calibration and energy scale for EC-EC events.

- 0.00013 due to energy smearing for EC-EC events.

9.2 Background estimation

Uncertainty from the background estimation is small due to a very tight selection cuts. For the MC estimated backgrounds including the EW and $W + jets$, the MC statistical uncertainties and the 4.2% relative uncertainty on the integrated luminosity are propagated into the final estimation. For the QCD multi-jets background, the statistical uncertainty in the shape taken from data, and the uncertainty from normalization fitting are considered. The systematic uncertainty on the extracted $\sin^2 \theta_W$ due to the backgrounds estimation is found to be 0.00002 for CC-CC, 0.00001 for CC-EC and 0.00002 for EC-EC events.

9.3 Charge mis-identification

Charge measurement is crucial to the analysis. But the systematic uncertainty from this part is negligible because the measured charge mid-identification probability is very small. The systematic uncertainty from this part is estimated using the statistical uncertainties in the mis-id measurement. We calculate the R in Eq. 6.8 with $f_{data} \pm 1\sigma$ and $f_{mc} \pm 1\sigma$. Then we apply the charge mis-ID correction with new values of R to MC. The final uncertainty on $\sin^2 \theta_W$ is 0.00002 for CC-CC, 0.00004 for CC-EC and 0.00012 for EC-EC.

9.4 Efficiency

Even though the A_{FB} distribution is a ratio measurement and the electron identification uncertainties in principle should cancel out, there are still some residual effects from electron identification. To estimate this uncertainty, we vary the preselection, electron ID and electron track match correction factors by $\pm 1\sigma$, and take the largest deviation on $\sin^2 \theta_W$ as uncertainty. The uncertainty from electron ID on $\sin^2 \theta_W$ is 0.00008 for CC-CC, 0.00008 for CC-EC and 0.00005 for EC-EC events.

9.5 PDFs uncertainty

The systematic uncertainty due to PDF is estimated using NNPDF2.3 [15] in the way suggested by the NNPDF collaboration. We reweight the PDF in the default MC to seven NNPDF2.3 sub-sets with α_s from 0.116 to 0.122 with a step of 0.001. Each sub-set has 100 different PDFs so totally 700 MC templates are generated. And we randomly chose 8 templates both from 0.116 and 0.122 sub-sets, 48 templates from both 0.117 and 0.121 sub-sets, 140 templates from both 0.118 and 0.120 sub-sets and 200 templates from 0.119 sub-set. For each chosen MC template, we observe the A_{FB} distribution as pseudo-data and measure the $\sin^2 \theta_W$

from it with the same χ^2 fitting method. Fig. 9.1 shows the measured $\sin^2 \theta_W$ values in all MC tempaltes.
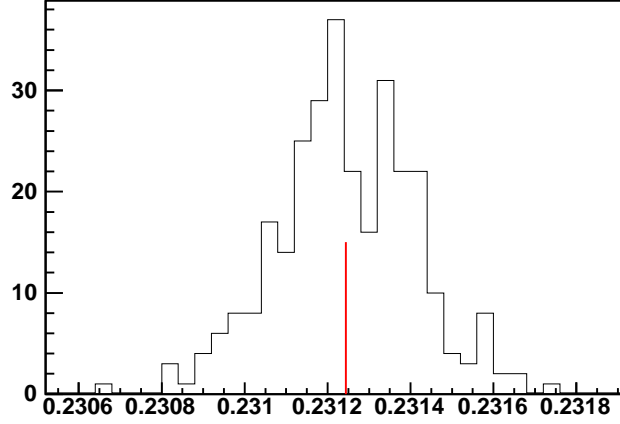

Figure 9.1: The measured $\sin^2 \theta_W$ values in all MC templates.

The PDF uncertainty is calculated as

$$S_0 = \frac{1}{N_{pdf}} \sum_{j=1}^{N_\alpha} \sum_{k_j=1}^{N_{\alpha(j)}} S(PDF^{(k_j,j),\alpha_s(j)})$$

$$\sigma = \sqrt{\frac{1}{N_{pdf}-1} \sum_{j=1}^{N_\alpha} \sum_{k_j=1}^{N_{\alpha(j)}} (S(PDF^{(k_j,j),\alpha_s(j)}) - S_0)^2}$$

where S_0 is the average $\sin^2 \theta_W$ value, $S(PDF^{(k_j,j),\alpha_s(j)})$ is the $\sin^2 \theta_W$ extracted from each MC template. The final result of σ is 0.00017.

9.6 Fiducial asymmetry

The polarities of the D0 solenoid magnet encompassing the tracking detectors and the iron toroid magnets in the muon system were reversed on a four week cycle that provided nearly equal luminosity exposure in each of the four solenoid/toroid polarity combinations. The potential asymmetry (if there is) will be perfectly cancelled if the statistics, or the integrated luminosity for the + solenoid - toroid, + solenoid + toroid, - solenoid + toroid and - solenoid - toroid samples are exactly the same. Thus, data samples can be weighted by the relative luminosity for each polarity combination. Combining these weighted samples allow substantial cancellation of the corrections to A_{FB} due to efficiency and acceptance variations across the tracking detectors and calorimeters.

We weighted the data sample for all solenoid/toroid polarities using their number of events. In the weighted sample, statistics for the four solenoid/toroid combinations are exactly the same. The weak mixing angle measured from the weighted data sample is shifted by 0.00001

compared to the original measured value. This shift is taken as the systematic uncertainty from the potential false asymmetry.

9.7   Final results

All the measurements and all systematic uncertainties are summarized in Tab. 9.1. The final result for the weak mixing angle from 9.1 fb^{-1} of RunIIb data is:

$$
\begin{aligned}
\sin^2 \theta_W &= 0.23147 \pm 0.00043(\text{stat.}) \pm 0.00008(\text{syst.}) \pm 0.00017(\text{PDF}) \\
&= 0.23147 \pm 0.00047
\end{aligned}
$$

The measured result, compared with other experiments' best precisions, is shown in Fig. 9.2.

	CC-CC	CC-EC	EC-EC	Combined
$\sin^2 \theta_W$	0.23142	0.23143	0.22977	0.23139
$\sin^2 \theta_l^{\text{eff}}$	-	-	-	0.23147
Statistical	0.00116	0.00047	0.00276	0.00043
Systematic	0.00009	0.00009	0.00019	0.00008
Energy Calibration	0.00003	0.00001	0.00004	0.00001
Energy Smearing	0.00001	0.00002	0.00013	0.00002
Background	0.00002	0.00001	0.00002	0.00001
Charge Misidentification	0.00002	0.00004	0.00012	0.00003
Electron Identification	0.00008	0.00008	0.00005	0.00007
Fiducial Asymmetry	0.00002	0.00001	0.00001	0.00001
PDF	-	-	-	0.00017
Total	0.00116	0.00048	0.00277	0.00047

Table 9.1: Measured weak mixing angle and corresponding uncertainties.
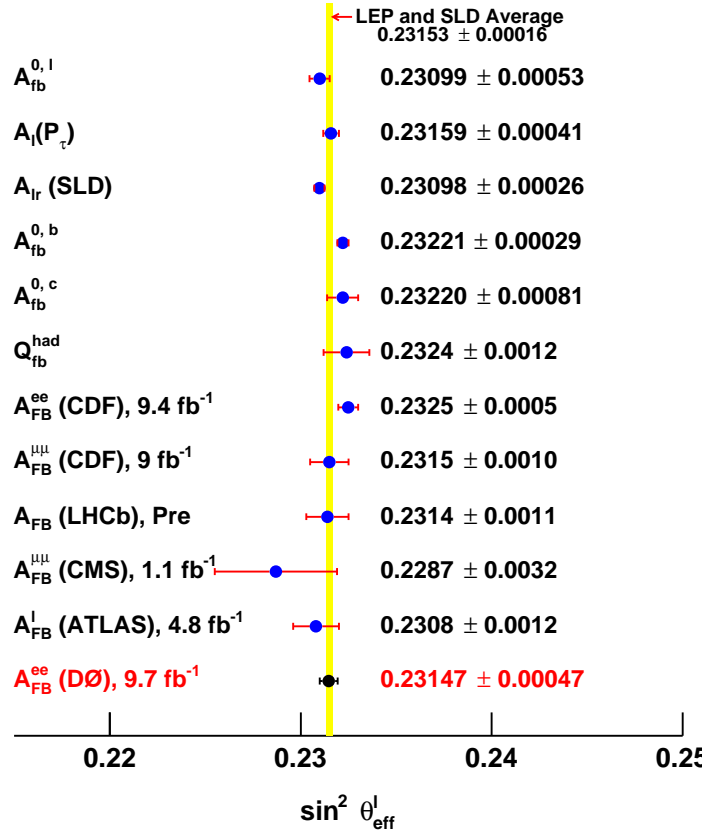
Figure 9.2: The D0 9.7 fb^{-1} electron channel result and measurements from other experiments.

Chapter 10

Conclusion

This thesis reports a measurement of the effective weak mixing angle $\sin^2 \theta_l^{\text{eff}}$ in $p\bar{p} \to Z/\gamma^* \to e^+e^-$ events, using the full data set corresponding to 9.7 fb^{-1} collected by the D0 experiment at the Fermilab Tevatron. The precision, estimated using the strategy and the results from the previous D0 5 fb^{-1} electron channel analysis once was 0.00081. However, it is significantly reduced by extending the acceptance of electrons which brings 80% more events. Most of the new electrons are poorly reconstructed so that they were excluded from the previous analysis. To keep a precise measurement of the weak mixing with such electrons, a new energy calibration method is developed and applied. As a results, the measured central value, together with uncertainties, is

$$
\begin{aligned}
\sin^2 \theta_l^{\text{eff}} = & \\
& 0.23147 \pm 0.00043 \, (\text{stat.}) \pm \\
& 0.00008 \, (\text{syst.}) \pm 0.00017 \, (\text{PDF}) \\
= \; & 0.23147 \pm 0.00047.
\end{aligned}
$$

It is the most precise determination of $\sin^2 \theta_l^{\text{eff}}$ from light quark interactions. It is also the first time that measurements of the weak mixing angle from hadron colliders can have a precision close to the world best results from the LEP b quark production and the SLD left-right polarization asymmetry.

References

[1] S.L. Glashow, Nucl. Phys. **B22** 579 (1961); A. Salam and J.C. Ward, Phys. Rev. Lett. **13** 168 (1994); S. Weinberg, Phys. Rev. Lett. **19** 1264 (1967). 1, 5

[2] The ALEPH, DELPHI, L3, OPAL, SLD Collaborations,the LEP Electroweak Working Group,the SLD Electroweak and Heavy Flavour Groups, Physics Reports, Volume 427 Nos. 5-6 (May 2006) 257-454.

[3] V. M. Abazov *et al.* (D0 Collaboration), Phys. Rev. Lett. **101**, 191801 (2008).

[4] V. M. Abazov *et al.* (D0 Collaboration), Phys. Rev.D **84**, 012007 (2011).

[5] J. C. Collins and D. E. Soper, Phys. Rev. D **16**, 2219 (1977).

[6] D. Acosta *et al.* (CDF Collaboration), Phys. Rev. D **71**, 052002 (2005).

[7] T. Aaltonen *et al.* (CDF Collaboration), Phys. Rev. D **88**, 072002 (2013).

[8] T. Aaltonen *et al.* (CDF Collaboration), Phys. Rev. D **89**, 072005 (2014).

[9] ATLAS collaboration, JHEP**09** (2015) 049

[10] S. Chatrchyan *et al.* (CMS Collaboration), Phys. Rev. D **84**, 112002 (2011).

[11] V. M. Abazov *et al.* (D0 Collaboration), Nucl. Instrum. Methods Phys. Res. A **565**, 463 (2006).

[12] M. Abolins *et al.* (D0 Collaboration), Nucl. Instrum. Methods Phys. Res. A **584**, 75 (2008).

[13] R. Angstadt *et al.* (D0 Collaboration), Nucl. Instrum. Methods Phys. Res. A **622**, 298 (2010).

[14] Ulich Baura, John Ellisonb and John Rhab, Report of the Working Group on Precision Measurements, arXiv:hep-ex/0011009

[15] R. D. Ball *et al.*, Nucl. Phys. **B867**, 244 (2013).

[16] T. Sjöstrand, P. Edén, C. Feriberg, L. Lönnblad, G. Miu, S. Mrenna, and E. Norrbin, Comp. Phys. Commun. **135**, 238 (2001). PYTHIA version v6.323 is used throughout.

[17] M. Mangano *et al.*, JHEP **0307**, 001 (2003).

[18] R. Bernhard, DØ note 5961.

[19] M. Anastasoaie, G.Bernardi, Y. Enari, F. Filthaut, W. Fisher, V. Kaushik, J. Lellouch, M. Sanders, L. Sonnenschein, J. Yu, DØ note 5357.

[20] V. M. Abazov *et al.* (D0 Collaboration), Nucl. Instrum. Meth. A **750**, 78 (2014).

[21] R. Engelmann, et al., Nuclear Instruments and Methods in Physics Research Section A 216 (1983) 45.

[22] S. Abachi, *et al.* (D0 Collaboration), Nuclear Instruments and Methods in Physics Research SectionA 324 (1993) 53.

[23] Xuebing bu, Herbert GreenLee. DØ note 6217.

[24] J. Humlicek, JQSRT, 21, 437 (1982).

[25] V. M. Abazov *et al.* (D0 Collaboration), Phys. Rev. D **89**, 012005 (2014).

[26] V. Abazov *et al.* (D0 Collaboration), Phys. Rev. D **76**, 012003 (2007).

[27] T. Nunnemann, DØ note 4476.

[28] R. Hamberg, W.L. van Neerven, and T. Matsuura, Nucl. Phys. B359, (1991).

[29] DØ note 4476.

[30] C. Balazs and C.P. Yuan, Phys. Rev. D56 (1997).

[31] S. Yacoob, J. Hays, H. Schellman, DØ note 5273.

[32] R. Hamberg, W.L. van Neevrven, and T. Matsuura, Nucl. Phys. B359, 343 (1991).

[33] J. M. Campbell and R. K. Ellis, Phys. Rev. D60, 113006 (1999).

[34] CDF Collaborations, Phys. Rev. Lett. 98, 161801 (2007).